



NAVAL POSTGRADUATE SCHOOL

MONTEREY, CALIFORNIA

THESIS

**STEADY AND UNSTEADY AERODYNAMIC FLOW
STUDIES OVER A 1303 UCAV CONFIGURATION**

by

Brian K. McLain

September 2009

Thesis Advisor:
Second Reader:

M. S. Chandrasekhara
G. V. Hobson

Approved for public release; distribution is unlimited

THIS PAGE INTENTIONALLY LEFT BLANK

DOCUMENTATION PAGE			<i>Form Approved OMB No. 0704-0188</i>	
Public reporting burden for this collection of information is estimated to average 1 hour per response, including the time for reviewing instruction, searching existing data sources, gathering and maintaining the data needed, and completing and reviewing the collection of information. Send comments regarding this burden estimate or any other aspect of this collection of information, including suggestions for reducing this burden, to Washington headquarters Services, Directorate for Information Operations and Reports, 1215 Jefferson Davis Highway, Suite 1204, Arlington, VA 22202-4302, and to the Office of Management and Budget, Paperwork Reduction Project (0704-0188) Washington DC 20503.				
1. AGENCY USE ONLY (Leave blank)		2. REPORT DATE September 2009	3. REPORT TYPE AND DATES COVERED Masters Thesis	
4. TITLE AND SUBTITLE Steady and Unsteady Aerodynamic Flow Studies over a UCAV 1303 Configuration			5. FUNDING NUMBERS	
6. AUTHOR(S) Brian K. McLain				
7. PERFORMING ORGANIZATION NAME(S) AND ADDRESS(ES) Naval Postgraduate School Monterey, CA 93943-5000			8. PERFORMING ORGANIZATION REPORT NUMBER	
9. SPONSORING /MONITORING AGENCY NAME(S) AND ADDRESS(ES) N/A			10. SPONSORING/MONITORING AGENCY REPORT NUMBER	
11. SUPPLEMENTARY NOTES The views expressed in this thesis are those of the author and do not reflect the official policy or position of the Department of Defense or the U.S. Government.				
12a. DISTRIBUTION / AVAILABILITY STATEMENT Approved for public release; distribution is unlimited			12b. DISTRIBUTION CODE	
13. ABSTRACT (maximum 200 words) <p>This study generated new information through qualitative documentation of the main flow features and direct measurements of the aerodynamic performance of a tailless, unmanned combat air vehicle (UCAV) 1303 configuration under both steady and unsteady maneuvering conditions. Photographic evidence of flow features, measurements of large-scale flow effects, and that of forces and aerodynamic coefficients during static and dynamic pitch, roll and yaw maneuvers were obtained. Flow visualization images and force measurements were taken at various Reynolds numbers, model attitudes and pitch rates for comparison.</p> <p>A 1/72nd-scale model with a 47-degree leading edge sweep and a cranked trailing edge delta wing with a fuselage was investigated in the NPS water tunnel. Phase locked, high-resolution flow images were obtained using a five color dye injection system over the maneuvering model. Both static and dynamic pitch-up, roll and yaw maneuvers were considered. Additionally, a five-component strain gage and flow monitoring software were employed to record, in real time, yawing, pitching and rolling moment information and derive the aerodynamic force and moment coefficients for selected maneuver conditions.</p> <p>Flow visualization revealed the presence of a strong spanwise flow at low angles of attack and strong vortical flow structures at larger angles of attack, as can be expected, but not clearly established earlier, for such low sweep angle wings. It also indicated that the vortical structures and reverse flow were highly Reynolds-number dependent. Normal force and pitching moment load data correlated well with trends observed for low sweep angle delta wings, but unexpected side force, yawing moment and rolling moment variations were observed, which were attributable to asymmetrical vortical flow behavior on the tailless UCAV geometry.</p>				
14. SUBJECT TERMS Unmanned Combat Air Vehicle, UCAV, UCAV 1303			15. NUMBER OF PAGES 77	
			16. PRICE CODE	
17. SECURITY CLASSIFICATION OF REPORT Unclassified	18. SECURITY CLASSIFICATION OF THIS PAGE Unclassified	19. SECURITY CLASSIFICATION OF ABSTRACT Unclassified	20. LIMITATION OF ABSTRACT UU	

THIS PAGE INTENTIONALLY LEFT BLANK

Approved for public release; distribution is unlimited

**STEADY AND UNSTEADY AERODYNAMIC FLOW STUDIES OVER A 1303
UCAV CONFIGURATION**

Brian K. McLain
Lieutenant, United States Navy
B.S., Ohio State University, 1999
M.S., Ohio State University, 2000

Submitted in partial fulfillment of the
requirements for the degree of

MASTER OF SCIENCE IN MECHANICAL ENGINEERING

from the

**NAVAL POSTGRADUATE SCHOOL
September 2009**

Author: Brian K. McLain

Approved by: M. S. Chandrasekhara
Thesis Advisor

G. V. Hobson
Second Reader

Knox T. Millsaps
Chairman, Department of Mechanical and Astronautical
Engineering

THIS PAGE INTENTIONALLY LEFT BLANK

ABSTRACT

This study generated new information through qualitative documentation of the main flow features and direct measurements of the aerodynamic performance of a tailless, unmanned combat air vehicle (UCAV) 1303 configuration under both steady and unsteady maneuvering conditions. Photographic evidence of flow features, measurements of large-scale flow effects, and that of forces and aerodynamic coefficients during static and dynamic pitch, roll and yaw maneuvers were obtained. Flow visualization images and force measurements were taken at various Reynolds numbers, model attitudes and pitch rates for comparison.

A 1/72nd-scale model with a 47-degree leading edge sweep and a cranked trailing edge delta wing with a fuselage was investigated in the NPS water tunnel. Phase locked, high-resolution flow images were obtained using a five color dye injection system over the maneuvering model. Both static and dynamic pitch-up, roll and yaw maneuvers were considered. Additionally, a five-component strain gage and flow monitoring software were employed to record, in real time, yawing, pitching and rolling moment information and derive the aerodynamic force and moment coefficients for selected maneuver conditions.

Flow visualization revealed the presence of a strong spanwise flow at low angles of attack and strong vortical flow structures at larger angles of attack, as can be expected, but not clearly established earlier, for such low sweep angle wings. It also indicated that the vortical structures and reverse flow were highly Reynolds-number dependent. Normal force and pitching moment load data correlated well with trends observed for low sweep angle delta wings, but unexpected side force, yawing moment and rolling moment variations were observed, which were attributable to asymmetrical vortical flow behavior on the tailless UCAV geometry.

THIS PAGE INTENTIONALLY LEFT BLANK

TABLE OF CONTENTS

I.	INTRODUCTION.....	1
A.	OVERVIEW.....	1
B.	BACKGROUND	3
1.	1303 UCAV Configuration	3
2.	Delta Wing Aerodynamics.....	3
3.	Lambda Wing Aerodynamics	5
C.	LITERATURE SURVEY	6
1.	Experimental	6
2.	Computational Fluid Dynamics	9
D.	OBJECTIVES	10
II.	EXPERIMENTAL APPARATUS AND TECHNIQUES.....	11
A.	WATER TUNNEL.....	11
1.	Model Support.....	12
B.	UCAV MODEL.....	12
C.	EXPERIMENTAL TECHNIQUES	14
1.	Method of Photography	14
2.	Flow Visualization	14
3.	Load Measurement	15
a.	<i>Internal Stain Gage Balance Calibration</i>	<i>16</i>
III.	FLOW VISUALIZATION ANALYSIS AND RESULTS	21
A.	FLOW VISUALIZATION.....	21
B.	STEADY MEASUREMENTS.....	21
1.	UCAV 1303 Configuration Flow.....	21
2.	Effect of Pitch	26
3.	Effect of Reynolds Number	31
4.	Effect of Roll Angle	34
5.	Effect of Yaw Angle.....	36
6.	Unsteadiness in LEV Breakdown	37
C.	DYNAMIC MEASUREMENTS	38
1.	Effect of Pitch Angle	38
2.	Effect of Roll Angle	41
3.	Effect of Yaw Angle.....	43
IV.	LOAD ANALYSIS AND RESULTS	45
A.	LOAD MEASUREMENT.....	45
B.	STATIC LOADING MEASUREMENTS	45
C.	DYNAMIC LOADING MEASUREMENTS	50
V.	CONCLUDING REMARKS.....	55
A.	SUMMARY OF RESULTS	55
B.	FUTURE WORK.....	56
	LIST OF REFERENCES.....	57
	INITIAL DISTRIBUTION LIST	59

THIS PAGE INTENTIONALLY LEFT BLANK

LIST OF FIGURES

Figure 1	Predator UAV, From [3]	2
Figure 2	Boeing 1303 UCAV, From [2]	3
Figure 3	Subsonic Flow Over a Delta Wing, From [10]	4
Figure 4	Spiral and Bubble Vortex Breakdown, From [13].....	5
Figure 5	Aerodynamic Properties versus AoA, From [7]	7
Figure 6	Variation of Lift Coefficient and Pitching Moment with Reynolds Number, From [4]	8
Figure 7	Naval Postgraduate School Water Tunnel Facility, From [19,20].....	11
Figure 8	NPS 15" x 20" water tunnel model support, From [20]	12
Figure 9	UCAV Model, From [20]	13
Figure 10	Flow Visualization Example.....	15
Figure 11	Five-component Internal Balance and Calibration Rig	17
Figure 12	Balance Response to a Positive Normal Force	18
Figure 13	Pitching Moment Sensitivity.....	19
Figure 14	Yawing Moment Sensitivity	20
Figure 15	Rolling Moment Sensitivity.....	20
Figure 16	Dye Visualization of Flow at $U_\infty=2$ [in/s], $Re=3.81 \times 10^3$	23
Figure 17	Transverse Dye Flow Visualization.....	24
Figure 18	Underside Flow Wrapping, $\alpha=15^\circ$, $U_\infty=2$ [in/s], $Re=3.81 \times 10^3$	25
Figure 19	Spiral and Bubble Type Breakdown Phenomena, $\alpha=12^\circ$, $U_\infty=2$ [in/s], $Re=3.81 \times 10^3$	25
Figure 20	Reverse Flow on UCAV 1303 $\alpha=10^\circ$, $U_\infty=6$ [in/s], $Re=1.17 \times 10^4$	26
Figure 21	Water Tunnel Velocity, $U_\infty=6$ [in/s], $Re=1.17 \times 10^4$	27
Figure 22	Recirculation Flow Regions, $\alpha=12^\circ$, $U_\infty=6$ [in/s], $Re=1.17 \times 10^4$	28
Figure 23	Side View, $\alpha=6^\circ$, $U_\infty=6$ [in/s], $Re=1.17 \times 10^4$	29
Figure 24	Vortex Breakdown Movement for the UCAV 1303 Configuration, $U_\infty=6$ [in/s], $Re=1.17 \times 10^4$	30
Figure 25	Reynolds Number Effect, $\alpha=6^\circ$	31
Figure 26	Vortex Breakdown Movement for the UCAV 1303 Configuration for Various Reynolds Numbers	32
Figure 27	Reynolds Number Effects with LEV Formation, $\alpha=10^\circ$	33
Figure 28	Variation in Spanwise Location of Vortex Core with Re	33
Figure 29	Roll single maneuver, $U_\infty=6$ [in/s], $Re=1.17 \times 10^4$	34
Figure 30	Combined Maneuver, $U_\infty=6$ [in/s], $Re=1.17 \times 10^4$	36
Figure 31	Effect of Yaw, $U_\infty=6$ [in/s], $Re=1.17 \times 10^4$	37
Figure 32	Wandering LEV Breakdown, $U_\infty=6$ [in/s], $\alpha=10.5^\circ$, $Re=1.17 \times 10^4$	38
Figure 33	Water Tunnel Velocity, $U_\infty=6$ [in/s], $Re=1.17 \times 10^4$, $\alpha=10^\circ$	39
Figure 34	Water Tunnel Velocity, $U_\infty=10$ [in/s], $Re=2.15 \times 10^4$, $\alpha=10^\circ$	40
Figure 35	Comparison of Pitch-up and Pitch-Down Maneuver, $U_\infty=6$ [in/s], $Re=1.17 \times 10^4$, $\alpha=10^\circ$, $\alpha^+=0.1$	41

Figure 36	Roll Rate Effects, $U_\infty=6$ [in/s], $Re=1.17 \times 10^4$, $\alpha=0^\circ$, $\phi=20^\circ$ Roll to Starboard.....	42
Figure 37	Combined Maneuver, $U_\infty=6$ [in/s], $Re=1.17 \times 10^4$, $\alpha=10^\circ$, $\phi=20^\circ$ Roll to Starboard.....	42
Figure 38	Yaw Rate Effects, $U_\infty=6$ [in/s], $Re=1.17 \times 10^4$, $\alpha=0^\circ$, $\beta=6^\circ$ Yaw to Port.....	43
Figure 39	Static Aerodynamic Coefficients, $U_\infty=6$ [in/s], $Re=1.17 \times 10^4$	47
Figure 40	Flow Visualization at Loading Points of Interest, $U_\infty=6$ [in/s], $Re=1.17 \times 10^4$	48
Figure 41	Static Aerodynamic Coefficients Variation with Re	49
Figure 42	Dynamic Loading Investigation Maneuver, $\alpha^+=0.1$	50
Figure 43	Dynamic Aerodynamic Coefficients, $U_\infty=6$ [in/s], $Re=1.17 \times 10^4$, $\alpha^+=0.1$	52
Figure 44	Static and Dynamic ($\alpha^+=0.1$) Coefficient Comparison, $U_\infty=6$ [in/s], $Re=1.17 \times 10^4$	54

LIST OF TABLES

Table 1.	Model Properties	14
Table 2.	Internal Strain Gage Balance Sensitivity	16
Table 3.	Calibration Output Matrix (lbf/V or in-lbf/V)	18
Table 4.	LEV Formation Location, $Re=1.17 \times 10^4$	30
Table 5.	Reynolds Number Effect on Observable Transverse Dye Flow	31

THIS PAGE INTENTIONALLY LEFT BLANK

ACKNOWLEDGMENTS

I would like to thank Professor M.S. Chandrasekhara for his exceptional guidance and wisdom during this investigation. His way of making the most difficult fluid flow concepts manageable made this work possible.

I would also like to thank Mr. Tom Christian and Mr. John Mobley of the Naval Postgraduate School, and Mr. Mike Kerho of the Rolling Hills Research Corporation without whose support this work would not be possible.

Last but not least, I would like to express my gratitude to my wife, Kristen Mary, daughters, Megan Marie and Amanda Rosalie, and son, Tyler Keith, who have supported me throughout my time at NPS. Their unwavering support and encouragement have made my thesis process enjoyable.

Acknowledgements are also due to the Singapore TDSI/Temasek Group for funding the project under grant no. TDSI/07-005/1A.

THIS PAGE INTENTIONALLY LEFT BLANK

ACRONYMS AND ABBREVIATIONS

AoA	=	Angle of Attack
b	=	Wing Span
c	=	Root Chord
\bar{c}	=	Mean Aerodynamic Chord
C_L	=	Lift Force Coefficient
C_M	=	Pitching Moment Coefficient
$C_{M,min}$	=	Minimum Pitching Moment Coefficient
C_N	=	Normal Force Coefficient
$C_{N,max}$	=	Maximum Normal Force Coefficient
C_R	=	Rolling Moment Coefficient
C_{YM}	=	Yawing Moment Coefficient
LEV	=	Leading Edge Vortex
M	=	Mach Number
N	=	Normal Force
PM	=	Pitching Moment
q	=	Dynamic Pressure
Re	=	Reynolds Number
RM	=	Rolling Moment
S	=	Side Force
s	=	Semi-span
U_∞	=	Free-stream Velocity
UCAV	=	Unmanned Combat Air Vehicle
YM	=	Yawing Moment
α	=	Angle Alpha; AoA
α^+	=	Non-dimensional Pitch Rate
$\dot{\alpha}$	=	Pitch Rate
β	=	Sideslip Angle
$\dot{\beta}$	=	Yawing Rate
μ	=	Fluid Viscosity

ρ = Fluid Density

ϕ = Roll Angle

$\dot{\phi}$ = Roll Rate

I. INTRODUCTION

A. OVERVIEW

The Unmanned Combat Air Vehicle (UCAV) concept is to develop an affordable weapon system that expands tactical mission options and provides a revolutionary new element in the air power arsenal [1]. The UCAV is a reusable aircraft controlled by operators located outside of the vehicle or by onboard computers that provide the capabilities of current manned aircraft. Therefore, UCAVs are expected to reliably participate in national defense roles of surveillance, strike and suppression of enemy air defense (SEAD). UCAVs exploit the design and operational freedoms associated with relocation of the pilot outside of the vehicle [1]. These freedoms provide advantages in the form of eliminating the threat of loss of human life, allowing the air vehicle to undertake more hazardous missions, operating with restrictions based on air vehicle performance and not human factors, and removal of onboard human safety and interface devices. As a result, the UCAV is smaller, lighter and has the ability to be designed to maximize stealth and aerodynamic capabilities.

Unmanned Air Vehicles (UAV) have been designed and operated throughout history, with reports dating back as early as World War I. These early combat UAVs, however, were really cruise missiles whose engine power would be cut after a certain number of revolutions so the aircraft would dive into its target [1]. UAV sophistication has increased with advances in technology that included radio frequency remote control and inclusion of high-powered jet engines. However, until the 1980s, UAVs were nothing but remote controlled airplanes capable of limited objectives. Until recently, UAVs were mostly used for intelligence, surveillance and reconnaissance missions (ISR), tasks for which they could provide the same results as conventional aircraft without risk of human casualty [2]. In this capacity, the UAVs required long range, low speed and low maneuverability [2]. With technological advancements, the offensive capabilities of UAVs were proven in February 2001, when the Hellfire-C laser guided anti-tank missile was successfully fired from the Predator UAV (Figure 1) [3]. As a UCAV, the first Predator with Hellfire missile mission was flown in October 2001, with the first

successful missile-firing mission completed in February 2002. Therefore, no longer were only manned aircraft required to engage and destroy targets discovered by reconnaissance aircraft [4]. UCAVs with increased stealth, speed and maneuverability requirements could perform the function of ensuring air superiority.



Figure 1 Predator UAV, From [3]

The next generation UCAV will be expected to extend upon the advances made by Predator. It must reliably perform national defense roles and adhere to specifications that demand unrestricted maneuverability. It will be expected to undertake rapid, large amplitude maneuvers, while maintaining control for destruction of enemy air defenses and safe return for future use. The next generation UCAV will also be expected to undertake slow speed reconnaissance missions that will span several days. Because it will be designed for high and low speed, high maneuverability and stealth requirements, designs are expected to focus on tailless flying aircraft, e.g., Boeing 1303 UCAV configuration (Figure 2). It is imperative, therefore, that the underlying flow physics and aerodynamics of a maneuvering UCAV is fully understood.



Figure 2 Boeing 1303 UCAV, From [2]

B. BACKGROUND

1. 1303 UCAV Configuration

The 1303 UCAV design originated at Boeing Phantom Works under contract to the Vehicles Directorate of the AFRL [4]. The 1303 configuration, with leading edge sweep of 47° , cranked trailing edge and aft-rounded tips is an abstracted representative of various UCAVs and blended wing-body configurations [5]. It is an edge-aligned or near-lambda delta wing that features a concave trailing edge crank at or near the mid-semi-span, and a convex trailing edge crank outboard, closer to the pointed wing tip [4]. The 1303 configuration, as conceived, included several novel design features including an offset weapons bay, offset engine and expandable fuel tank [6].

Original development and design of the 1303 UCAV configuration began with selection of the 1301 UAV by Boeing Phantom Works with modifications to improve anticipated performance and align the configuration with future vehicles requirements [7]. These modifications included decreasing the leading edge angle from 50 degrees to 47 degrees, increasing the trailing edge angle from 20 degrees to 30 degrees and increasing the aspect ratio from 3.07 to 3.85 [7].

2. Delta Wing Aerodynamics

As a variant of a delta wing, the 1303 UCAV configuration is expected to exhibit aerodynamic properties commonly associated with traditional delta wings. This includes a primary aerodynamic flow pattern dominated by the formation of two vortex patterns

generated on the upper surface of the wing in the vicinity of the highly swept leading edges at sufficiently high angles of attack [8]. Figure 3 shows a schematic of the subsonic flow field over the top of a delta wing with generation of leading edge vortices. The counter-rotating vortices are generated when the wing is at sufficient AoA since the pressure on the bottom surface of the wing is higher than the top surface of the wing. With a sharp leading edge, flow shear layers will separate along its entire length due to the inability to negotiate the sharp corner and will curl into a primary vortex that exists just inboard and above the wing surface. [9,10,11]. The leading edge vortices are primary vortices and are the dominant features of the flow across a delta wing, however, secondary and tertiary vortex formation often occurs. Secondary vortices differ from their primary counterpart in that flow separation is not fixed geometrically along a separation line; secondary separation is highly Reynolds number dependent and is caused by local boundary layer separation [11].

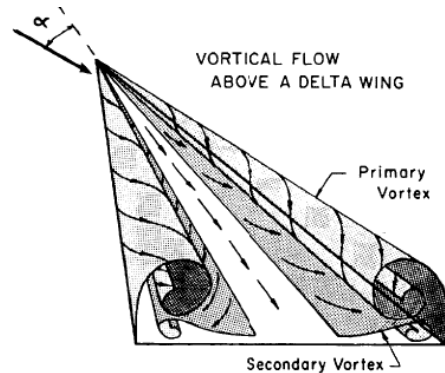


Figure 3 Subsonic Flow Over a Delta Wing, From [10]

The leading edge vortices generated by the delta wing are strong and stable [9]. The vortices are sources of high energy with very high speeds that create low local surface pressure. Vortices are able to produce axial speeds as high as two to three times the freestream velocity [11]. The difference in pressure from the bottom surface to the top surface of the delta wing produces additional lift, known as vortex lift. The additional lift is a significant advantage over conventional rectangular wings. The vortex lift increases with increasing AoA [8]. This is due to the fact that at larger angles of attack, vortex strength and vortex diameter increases are observed, that result in lower pressure and a large increase in axial velocity [2].

The beneficial lift generated by the formation of leading edge vortices however, ends abruptly at a critical value of AoA. At the critical value, which corresponds to a large AoA, the leading edge vortices experience an abrupt change with an increase in dynamic pressure and loss of axial velocity, this is vortex breakdown or vortex burst [8]. As AoA is increased further, beyond the critical value, the location of vortex breakdown moves upstream ultimately leading to stall conditions as the vehicle lift drops significantly [8].

Vortex breakdown is a violent phenomenon that involves: a rapid deceleration of the vortex core in the streamwise direction, a rapid increase in vortex diameter, a possible region of reversed flow and degradation of the vortex into a wave-like turbulent flow with no coherent structure [11]. Vortex breakdown has been cataloged into four basic breakdown modes: bubble breakdown, spiral breakdown, double helix breakdown, and conical breakdown [12]. However, bubble (bottom streak) and spiral breakdown (top streak) are the two most common vortex breakdown modes described in aerodynamic literature and are shown in Figure 4. Regardless of type of vortex breakdown, there is an adverse affect on the performance of the wing including a decrease in the magnitude of the lift and pitching moment.

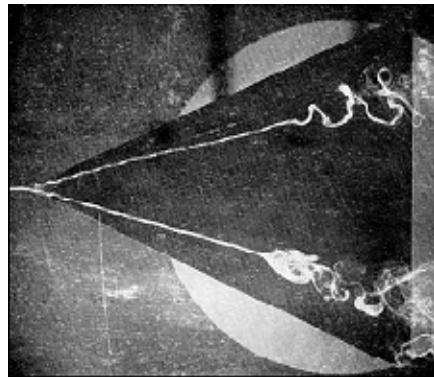


Figure 4 Spiral and Bubble Vortex Breakdown, From [13]

3. Lambda Wing Aerodynamics

As a near-lambda wing with concave trailing edge crank at the mid-section and concave trailing edge crank outboard, the 1303 UCAV configuration geometry combines increased aspect ratio and taper with planform edge alignment, relative to a single-panel

swept-tapered wing [4]. The trailing edge cranks affect and can cause problems with aerodynamic performance. The outboard crank generates a local minimum in the section lift coefficient [4]. The local minimum in chord associated with the inboard trailing edge crank results in a local maximum in section lift coefficient, while another maximum in section lift coefficient exists between the outboard crank and the tip, where loading goes to zero [4]. Therefore, the peak local lift coefficient occurs either at the inboard crank or slightly inboard of the wing tip [4].

It is expected that flow separation will occur at or near either of the local maximum section lift coefficients [4]. With flow separation at or near the inboard crank, fully separated flow over the outboard wing panel is expected due to movement of flow separation from the onset location [4]. As a result, the centroid of lift changes location, moving inboard and forward. The lambda wing, therefore, can experience undesirable pitch-up behavior.

C. LITERATURE SURVEY

1. Experimental

The 1303 UCAV configuration as selected by Boeing Phantom Works was initially tested during the selection process to enable stability and control database development and to allow flight performance assessment [7]. These studies evaluated the aerodynamic performance for speeds corresponding to values between Mach number 0.45 to Mach number 1.4 in the Boeing Polysonic Wind Tunnel, for angles of attack -2° to 20° . During the high-speed wind tunnel testing of Billman and Osborne [7], it was noted that there was development of a strong vortical flow structure along the leading edge and that at angles of attack between four and eight degrees (for $M=0.6$), the vortex rotates off the leading edge and sweeps across the outboard wing panel [7]. The Boeing Phantom Works project determined lift coefficient, drag coefficient and pitch moment coefficient for the 1303 UCAV configuration (Figure 5), but the study was limited to angles of attack less than twenty degrees. The study, however, revealed apparent stall with associated loss of lift at an AoA of nineteen degrees (for $M=0.45$), but in general the angles of attack were too low to observe stall for other values of Mach number.

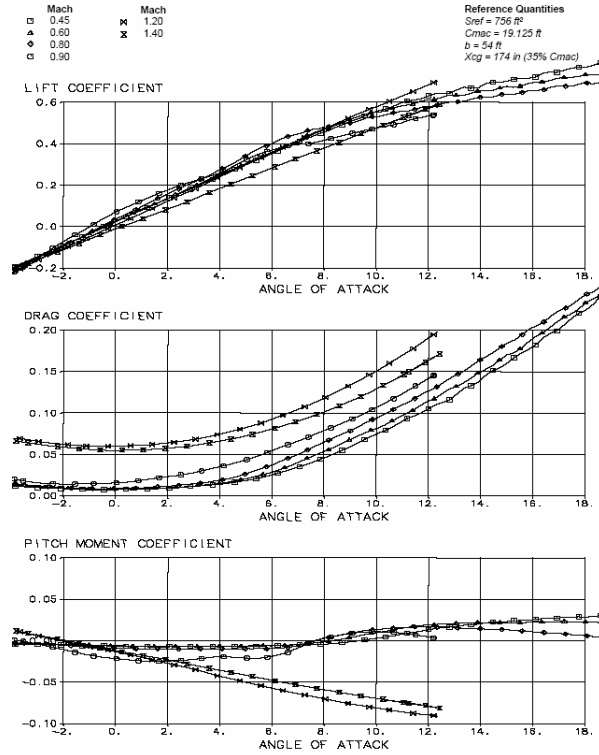


Figure 5 Aerodynamic Properties versus AoA, From [7]

In these results, it is observed that the lift coefficient is linear up to approximately 12° after which the slope decreases slightly. The drag coefficient is fairly constant to approximately 2° with a minimum that occurs at an AoA of 0° and then rapidly increases with AoA. The pitching moment results show a constant pitching moment value at angles of attack from approximately -2° to 8°, and then an increase as AoA is increased to 20°.

Low speed wind tunnel tests were conducted in the QinetiQ 5-meter pressurized low-speed wind tunnel. In this study, McParlin et al. [4] measured the lift coefficient, drag coefficient and pitching moment coefficient and presented these measurements as a function of Reynolds number and Mach number. The results, Figure 6, show a pitch-up behavior of the 1303 UCAV configuration at angles of incidence below 10°.

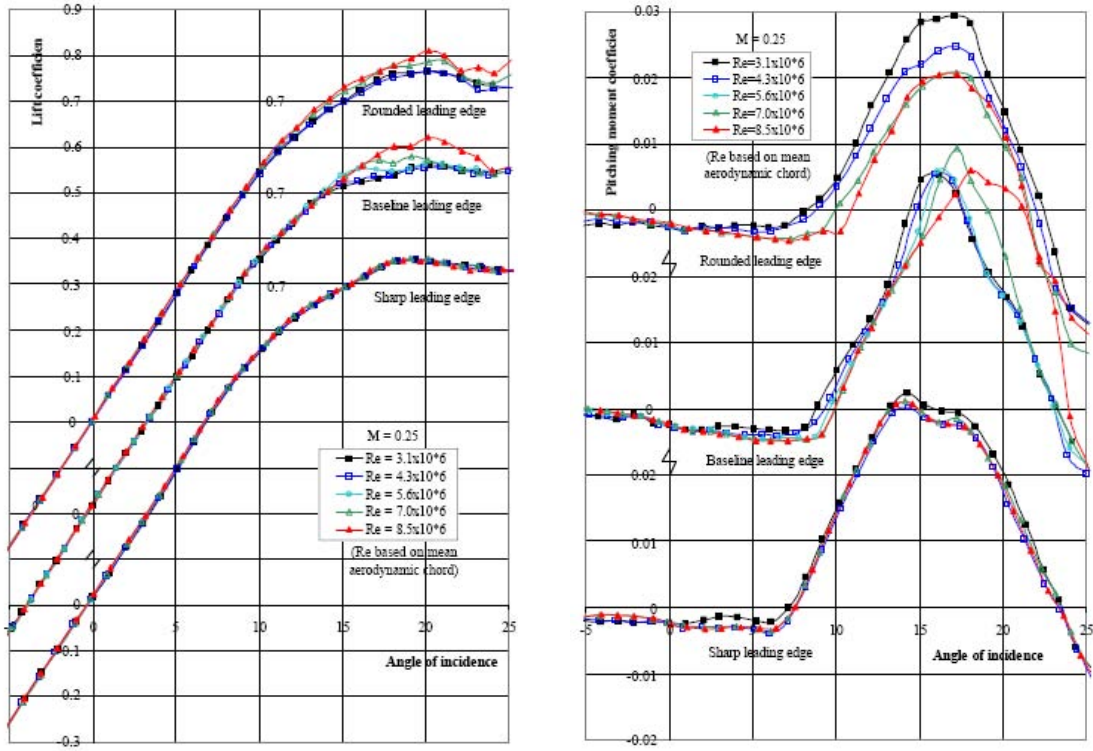


Figure 6 Variation of Lift Coefficient and Pitching Moment with Reynolds Number, From [4]

As an alternative to costly wind tunnel testing, 1303 UCAV configuration testing was completed in water tunnels with remarkable results. Ol [5] tested a sharp leading edge configuration demonstrating that tip stall was a leading contributor to pitch-break phenomenon and suggested that the LEV system was weak and unlikely to be a strong contributor to pitch-break. Due to previous work on 50°-sweep delta wings that indicated maximally unsteady wandering of LEVs, Ol focused this study on $\alpha=12^\circ$. This study provided evidence of only a single isolated existence of LEV formation.

Nelson et al. [14] utilized a water tunnel flow visualization technique over a half-span model to document flow results. In this study, at $\alpha < 7^\circ$, dye patterns indicated flow dominated by mean cross-flow from the wing root to the wing tip. It further indicated that at $\alpha > 8^\circ$, dye patterns indicated the formation of LEV. In contrast to the results of Ol

[5], LEV formation was particularly evident at $\alpha=12^\circ$. The results of this study also indicated that the flow was dominated in the inboard span by a LEV and outboard span by leading edge flow separation [14].

Kosoglu and Rockwell [15] further investigated the flow structure around the UCAV 1303 configuration using a water tunnel facility. In this investigation, dye visualization and particle image velocimetry were utilized at various Reynolds number flows and angles of attack. Results indicated that there was evidence of LEV formation at AoA as low as 6° and that there was indication of tip stall at all angles of attack investigated [15]. It further showed that the stall moves upstream and inboard as AoA is increased.

Thus, it appears that there have been some contradictions in the literature on the nature of the flow field surrounding the UCAV 1303 configuration. This includes formation and effect of LEV, vortex breakdown and pitch-up phenomenon which points to the need for further studies to resolve these points.

2. Computational Fluid Dynamics

CFD studies have been conducted to assess the performance of the UCAV 1303 configuration in an effort to validate current CFD code, compare CFD code between countries and provide insight into the expected flow field surrounding the 1303 configuration. In most cases, the CFD results were compared to results obtained in the QinetiQ 5-meter low speed wind tunnel.

Zhang et al. [16] performed a computational study of the aerodynamic performance of a UCAV 1303 configuration with baseline profile, a rounded leading edge and sharp pointed front profile. Computational results showed that flow remains smooth and attached at low angles of attack, that a vortex begins to grow along the swept leading edge at $\alpha=7^\circ$ with $M=0.25$ and that the vortex continues to grow in intensity as AoA increases [16].

Further studies conducted by Wong and Flores [17] and Chung and Ghee [18] similarly compared baseline and sharp leading edge models. These investigations were in close agreement providing C_L , C_D , C_M , L/D and flow visualization for angles of attack

between 0° and 14° . Atkinson and Ferguson [8] provided a computational fluid dynamics investigation to provide validation of UCAV 1303 aerodynamic properties for angles of attack between 0° and 14° . The work of Atkinson and Ferguson acknowledges that at this point the nature of the flow field around the UCAV 1303 configuration is questionable [8].

D. OBJECTIVES

The next generation UCAV will require unrestricted maneuvering to perform the requisite national defense role for which it is being designed. It is imperative, therefore, that the steady and unsteady aerodynamics on the rapidly maneuvering UCAV be fully understood. To this end, the larger study of which this thesis is a part will provide relevant information on UCAV aerodynamics especially for lower speed and maneuver conditions.

In the past, research on the UCAV 1303 configuration has been limited in scope to CFD validation of results seen in wind tunnel experiments, low speed or low AoA experimental studies. Further, there has been contradiction in the literature on the nature of the flow field surrounding the UCAV 1303 configuration. This includes formation and effect of LEV, vortex breakdown and pitch-up phenomenon.

The research in this study builds on previous research conducted on the 1303 UCAV configuration with an ultimate goal of controlling the unsteady aerodynamics of the rapidly maneuvering UCAV. The objectives of this study are: to determine the flow field developed around a 1303 UCAV configuration during steady and unsteady maneuvers such as pitch-up, roll and combined maneuvers, to determine the resulting loads as measured by a multi-component strain gage balance on the UCAV during such maneuvers and to determine if the aerodynamic performance provides critical dynamic stall information.

II. EXPERIMENTAL APPARATUS AND TECHNIQUES

A. WATER TUNNEL

The experiments of this study were conducted in the Naval Postgraduate School flow visualization water tunnel facility. Designed by Eidetics International, Inc., and installed in 1988, it is a closed circuit facility capable of studying a wide range of aerodynamic and fluid dynamic phenomena [19]. Figure 7 shows the schematic configuration and photograph of the Naval Postgraduate School Model 1520 water tunnel facility.

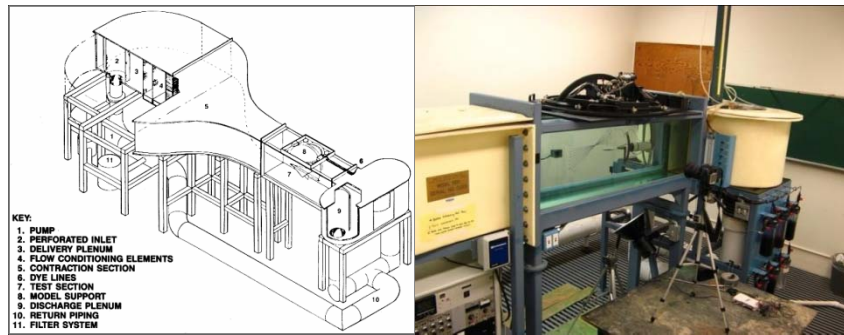


Figure 7 Naval Postgraduate School Water Tunnel Facility, From [19,20]

The NPS water tunnel offers continuous operation, high flow quality, horizontal orientation, adjustable flow rate and a visible test section. Horizontal orientation facilitates access, and enables models to be readily changed without draining the water from the tunnel [21, 22, 23]. Water circulation rates as high as 900 gallons/minute is possible providing in excess of 1 foot/sec flow rate in the visible test section.

The visible test section is constructed of scratch resistant tempered glass. This section is nominally 15 inches wide, 20 inches high, and 60 inches long with sidewalls that have a slight divergence to compensate for boundary layer growth and to provide uniform flow velocity throughout [19]. The test section and discharge plenum are designed to provide simultaneous viewing from the bottom, sides and rear. Additionally, the test section is designed with an open top to facilitate quick model insertion, removal and adjustment.

1. Model Support

The model support system is depicted in Figure 8. The model support system provides automatic control to allow steady roll, yaw and pitch angles, as well as dynamic control of the model during tunnel operation. The model is supported from the top of the tunnel using a C-strut to change pitch angle and turntable to change yaw angle. The roll mechanism is a waterproofed cylindrical support attached to the C-strut that permits roll motion. Three remotely driven DC motors vary the model attitude (roll, pitch and yaw) [19]. As configured within the NPS 15" x 20" water tunnel for this investigation, the C-strut and roll mechanism arrangement allows -1° to 40° pitch-up motions, $\pm 360^\circ$ roll motions and $\pm 30^\circ$ yaw motions.

The model control system was driven using PC based LABVIEW software programmed to simultaneous control roll, pitch and yaw position, as well as tunnel fluid velocity. To prevent interference with surface effects, the model is mounted with a sting and upside down in the visible test section. The model is removed from the test section when not in use and is accessed by rotation of the model support platform about hinges attached to a permanent base plate.

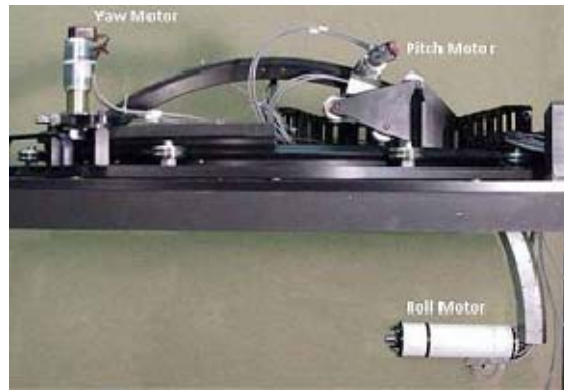


Figure 8 NPS 15" x 20" water tunnel model support, From [20]

B. UCAV MODEL

Two $1/72^{\text{nd}}$ -scale 1303 UCAV models with fuselage were used for this investigation; one model consisted of dye ports for steady and dynamic flow visualization study, while the other model housed the five-component internal strain gage balance for steady and dynamic loading study. The models were fabricated out of nylon 12PA with a

smooth polyurethane coat finish. Figure 9 is a representative photo of the models used for this investigation. The model shape was a thin flat model based on the single engine UCAV 1303 configuration. The models consist of a leading edge sweep of 47° , trailing edge sweep of $\pm 30^\circ$ and $\pm 47^\circ$. Both models were identical in planform area, span and mean aerodynamic chord. The aerodynamic properties of the models utilized are presented in Table 1.



Figure 9 UCAV Model, From [20]

The flow visualization model (Figure 9) was fabricated in a single piece and consisted of eight symmetrically located dye ports (four per side) placed at $0.05c$, $0.11c$, $0.22c$ and $0.33c$, with two placed to capture the critical region of wing body junction. Additionally, a dye port was located underneath the starboard leading edge along the wing. Dye tubes were routed through the interior of the model, with the exception of the lower dye port, which remained external to the model under investigation and allowed movement for further investigation. Model dye ports were approximately 0.5mm in size.

The load study model was fabricated in two pieces and housed a waterproofed internal balance to measure normal force (N), side force (S), pitching moment (PM), rolling moment (RM) and yawing moment (YM). The two-piece design facilitated placement of the internal balance at the aerodynamic center and ensured proper fit.

<u>Model Property</u>	<u>Value</u>
A_{ref}	21.11 in ²
b	9 in
c	5.34 in
\bar{c}	3.54in

Table 1. Model Properties

C. EXPERIMENTAL TECHNIQUES

1. Method of Photography

The equipment used for the photographic sessions consisted of two Nikon D80 digital SLR cameras and two floodlights located below the water tunnel test section. The cameras were operated in program mode with manual focus to maintain a constant focal length at the center of dye flow. The side view camera was maintained inline with the model at zero pitch angle, while the top view camera was maintained at a slight angle to provide continuous view of the flow field regardless of pitch, roll or yaw angle.

2. Flow Visualization

Five pressurized dye canisters using water-soluble food coloring were used for flow visualization. Each canister was pressurized with air by a small compressor and connected to the model port through an individually routed line [19]. The water-soluble food coloring was diluted with tap water in the ratio 1:4 to provide good contrast for flow visualization studies. The use of a pressurized system allowed finer control of dye emission.

Although it was initially expected that large quantities of dye would be required for flow field visualization, experimental investigation showed that large dye flow rates tended to push the dye away from the surface, especially notable at large AoA. Further, it was recognized that the effects of dye injection had to be minimized to allow accurate visualization of the flow field around the models under investigation. Therefore, in addition to the flow control gained through the use of the pressurized system, the dye

lines from the pressurized canisters contained flow control valves to provide dye flow adjustment capability. This enabled the quantity of dye to be carefully adjusted such that optimal dye flow was used for each experimental run, ensuring that dye flow remained sufficiently close to the surface.

Due to the symmetrical nature of the model under investigation, the dye flow lines to the model were split following flow control, providing the same dye color to symmetrically similar ports located along the model's leading edge and just below the wing surface. Figure 10 provides an example of the flow visualization produced within this investigation. For this investigation, color sequence was maintained to allow easy cross-reference with later experimental trials.

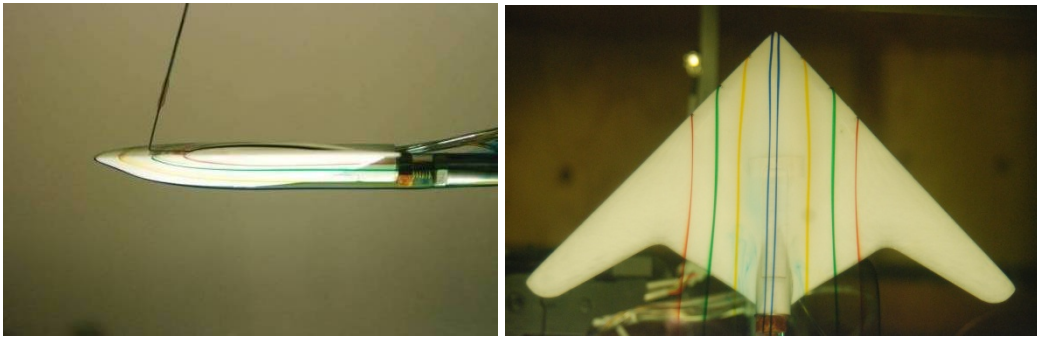


Figure 10 Flow Visualization Example

3. Load Measurement

Load measurement was accomplished using a five-component internal balance allowing simultaneous measurement of normal and side forces, as well as pitching, rolling and yawing moments. The internal balance consisted of a single rolling section (RM), two pitching moment sections (PM1 and PM2) and two yawing moment sections (YM1 and YM2) [21]. All sections were 1.91 cm (3/4") in diameter [21]. Each section used four semiconductor strain gages connected using a full Wheatstone bridge. The strain gages were 1000 Ω semiconductor gages with a gage factor of 145 that provided measurement for maximum loading of 15 in-lbs in the pitch plane moment, 4 in-lbs maximum loading in the yaw plane moment and 2.5 in-lbs of torque [23]. Table 2 shows the internal balance sensitivities. The balance was waterproofed using a combination of thin plastic coating and RTV (silicone rubber) to allow adequate functionality in a water-

submerged environment. The internal balance signals generated during testing are conditioned and balanced using an eight-channel Model 2100 Strain Gage Conditioner and Amplifier. The output lines are filtered and sent to a National Instruments PCI-MIO-16XE-10 S/D conversion board that provides guaranteed rates up to 100 kilo-samples/sec per channel before processing by the data acquisition/reduction software [23].

<u>Force/Moment</u>	<u>Sensitivity</u>
N	2.4 V/lb
S	16.8 V/lb
PM	5.0 V/in-lb
RM	10.2 V/in-lb
YM	16.4 V/in-lb

Table 2. Internal Strain Gage Balance Sensitivity

a. Internal Stain Gage Balance Calibration

The balance was calibrated to ensure accurate and repeatable response of each of the five sections to loads in its primary plane of action (sensitivity), as well as to loads in other planes of actions (interactions) [21]. The full calibration procedure was completed using the calibration rig and loading fixture shown in Figure 11, with a loading schedule that ensured the full range of expected loads were tested. The calibration rig consisted of an aluminum support where the sting and balance are attached, pulleys on each side of the balance and loading fixture attached to the end of the internal balance [21]. Loads were applied at five load points (LP1, LP2, LP3, LP4 and LP5) along the loading fixture with positive and negative normal and side forces, and at the balance reference center with positive and negative rolling moments [21]. The data acquisition/reduction software acquired the loading data, graphed the data, applied a linear curve fit and generated the calibration output matrix necessary to transform measured yawing, pitching and rolling moments from the five strain gage sections into normal and side forces, as well as pitching, yawing and rolling moments at the balance

center using Equation (1). The calibration output matrix is shown in Table 3. The balance calibration procedure was conducted and verified per the procedures and graphs of Suarez et al. [21], as presented below.

Calibration Output Matrix

$$\begin{bmatrix} N \\ PM \\ S \\ YM \\ RM \end{bmatrix} = \begin{bmatrix} \frac{\partial N}{\partial YM1} & \frac{\partial N}{\partial PM1} & \frac{\partial N}{\partial RM} & \frac{\partial N}{\partial PM2} & \frac{\partial N}{\partial YM2} \\ \frac{\partial PM}{\partial YM1} & \frac{\partial PM}{\partial PM1} & \frac{\partial PM}{\partial RM} & \frac{\partial PM}{\partial PM2} & \frac{\partial PM}{\partial YM2} \\ \frac{\partial S}{\partial YM1} & \frac{\partial S}{\partial PM1} & \frac{\partial S}{\partial RM} & \frac{\partial S}{\partial PM2} & \frac{\partial S}{\partial YM2} \\ \frac{\partial YM}{\partial YM1} & \frac{\partial YM}{\partial PM1} & \frac{\partial YM}{\partial RM} & \frac{\partial YM}{\partial PM2} & \frac{\partial YM}{\partial YM2} \\ \frac{\partial RM}{\partial YM1} & \frac{\partial RM}{\partial PM1} & \frac{\partial RM}{\partial RM} & \frac{\partial RM}{\partial PM2} & \frac{\partial RM}{\partial YM2} \end{bmatrix} \bullet \begin{bmatrix} YM1 \\ PM1 \\ RM \\ PM2 \\ YM2 \end{bmatrix} \quad (1)$$

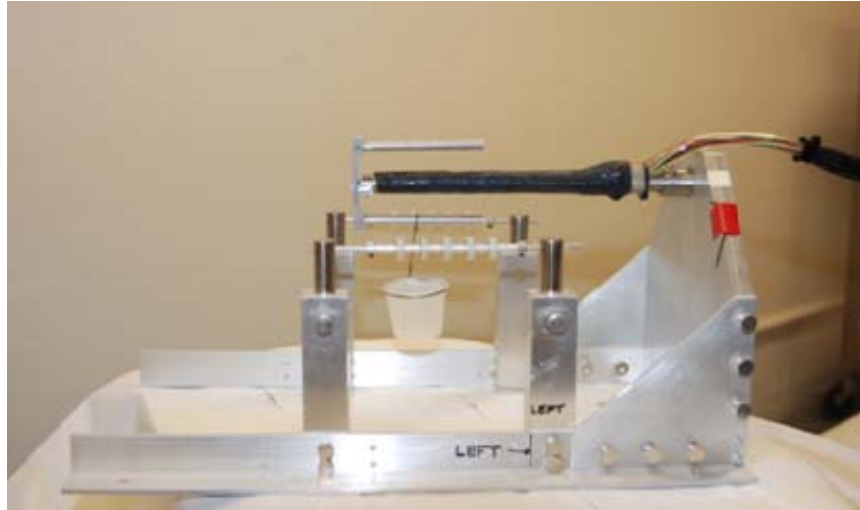


Figure 11 Five-component Internal Balance and Calibration Rig

<u>YM1</u>	<u>PM1</u>	<u>RM</u>	<u>PM2</u>	<u>YM2</u>
-3.62×10^{-2}	$-4.02 \times 10^{+1}$	-1.32	$4.06 \times 10^{+1}$	2.06×10^{-2}
-4.39×10^{-3}	$2.18 \times 10^{+1}$	-1.99×10^{-1}	$1.84 \times 10^{+1}$	2.76×10^{-2}
-5.74×10^0	2.08×10^{-1}	-1.11×10^{-1}	-1.77×10^{-1}	6.25×10^0
6.05×10^0	1.07×10^{-2}	-2.20×10^{-1}	-1.04×10^{-1}	6.14×10^0
-6.18×10^{-1}	8.99×10^{-1}	$-1.99 \times 10^{+1}$	-1.33×10^0	4.63×10^{-1}

Table 3. Calibration Output Matrix (lbf/V or in-lbf/V)

Figure 12 shows the results of a calibration loading case with a positive normal force applied at the loading point located 2.4" from the front of the internal balance (LP 4). This figure presents an indication of balance channel sensitivity and interactions between channels to the applied load under consideration. It is observed that the largest response is shown by PM1, as expected, since the normal force produces a pitching moment and this is the most forward pitching moment section [21]. Negligible response is observed seen at PM2 since this is the location of loading point and therefore does not react [21]. Figure 12 also displays negligible response of the RM channel and small response in each of the YM channels. Similar results were obtained for loads and moments applied in other directions.

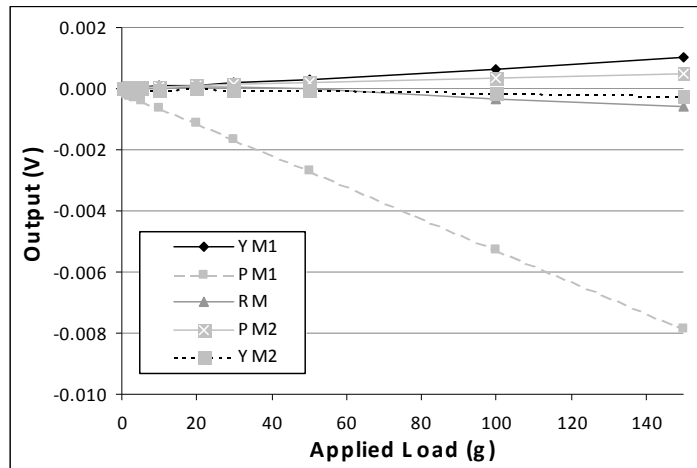


Figure 12 Balance Response to a Positive Normal Force

As an additional validation of the procedures implemented by the data acquisition/reduction software calibration, the slopes of the output of each channel at different load points are plotted in Figure 13, Figure 14 and Figure 15. Figure 13 is the response of the pitching moment strain gages to an applied pitching moment [21]. The slopes are the sensitivity of these channels to an applied pitching moment, while the y-intercept is the sensitivity of these channels to an applied normal force [21]. It is observed that channel outputs when plotted are linear with applied load and therefore, the linear approximation of the data acquisition/reduction software is justified. Figure 14 is the response of the yawing moment strain gages to an applied yawing moment, with slopes and intercepts providing similar measures for applied yawing moment and applied side force. Figure 15 is the response of the rolling moment section to the application of an applied rolling moment. It is observed that this response is linear for positive or negative applied rolling moment and the slope represents the sensitivity of the RM section to an applied rolling moment [21].

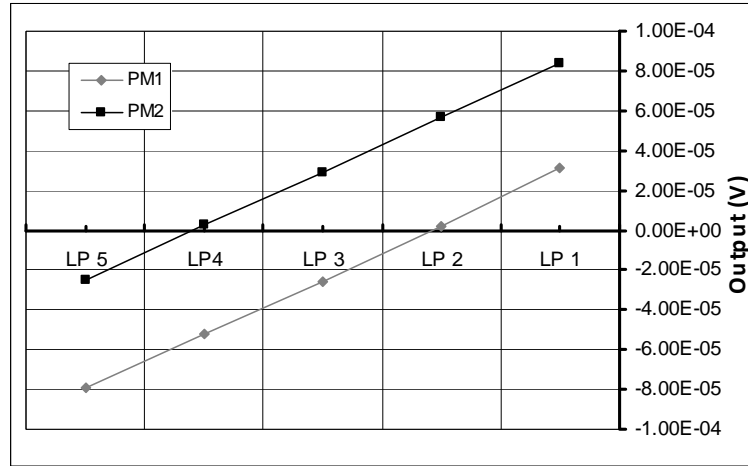


Figure 13 Pitching Moment Sensitivity

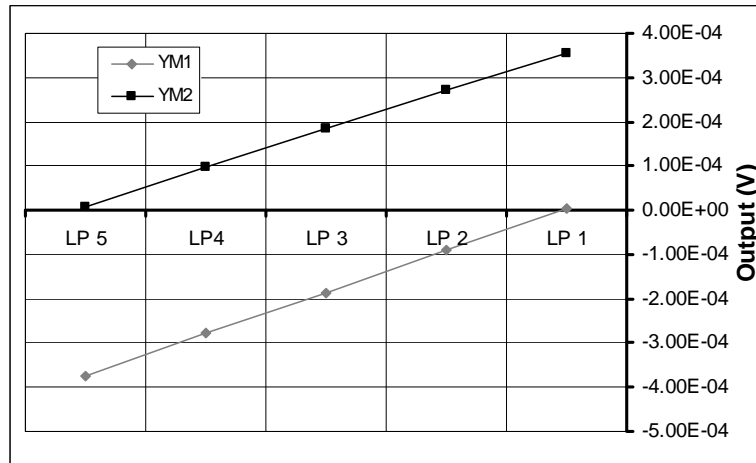


Figure 14 Yawing Moment Sensitivity

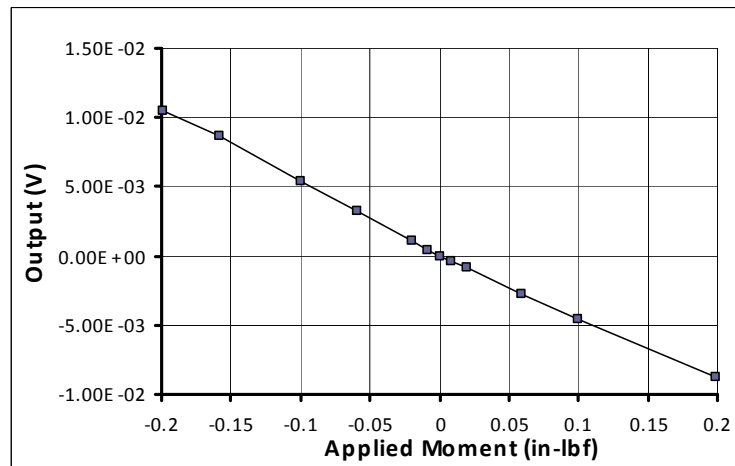


Figure 15 Rolling Moment Sensitivity

III. FLOW VISUALIZATION ANALYSIS AND RESULTS

A. FLOW VISUALIZATION

Dye flow visualization technique was utilized to document the flow field around the maneuvering UCAV 1303 configuration during steady and dynamic maneuvers. This technique consisted of injecting water-soluble food coloring from the previously indicated stations to highlight the flow around the UCAV model to provide a qualitative description of UCAV flow features. Flow visualization allowed observation of general flow characteristics, LEV formation, vortex trajectory, vortex bursting and reverse flow.

It is well established that a properly prepared dye mixture is neutrally buoyant and that it follows the flow streamlines over the UCAV model and also follows the vortex trajectory. Therefore, dye visualization can provide indications of LEV formation and associated vortex trajectory. Further, by introducing changes in pitch angle, roll angle, yaw angle or Reynolds number the effect on vortex formation and trajectory is observable through flow visualization techniques. Since the dye is entwined in the flow of vortices on the wing, vortex bursting is visible using this technique, as a breakdown of the flow along the wing.

B. STEADY MEASUREMENTS

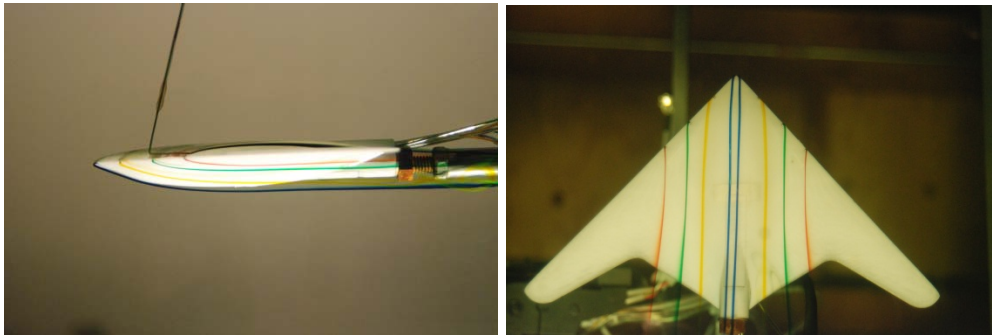
Steady flow visualization was performed in an effort to describe the flow field around the UCAV 1303 configuration, under various steady flow conditions of Reynolds number and pitch, roll, and yaw-angles. During the steady runs, the flow field was permitted time to stabilize prior to taking photographic evidence. The steady flow visualization was undertaken to augment previous results, as well as to clarify conflicting results reported for the UCAV 1303 configuration, to provide visual evidence of flow field physics for UCAV 1303 configuration with associated fuselage, and to provide a foundation for future analysis.

1. UCAV 1303 Configuration Flow

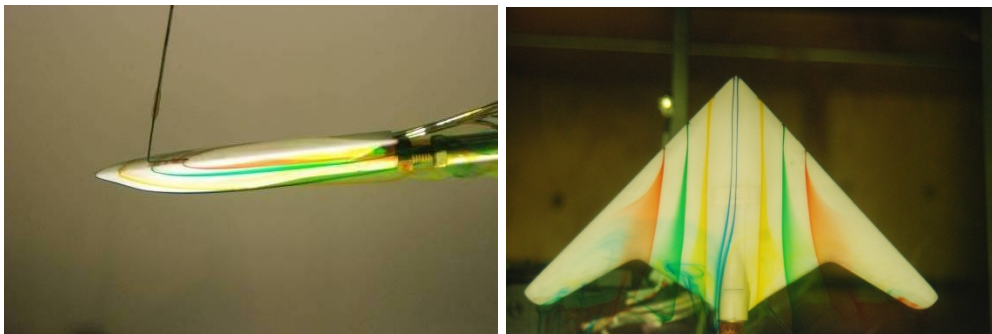
Preliminary water tunnel test runs showed clearly that the flow around the UCAV 1303 configuration is complex and dependent on the pitch angle, roll angle, yaw angle

and Reynolds number. It further showed that the flow field around the UCAV 1303 configuration displayed similarities and differences from traditional delta wing expectations.

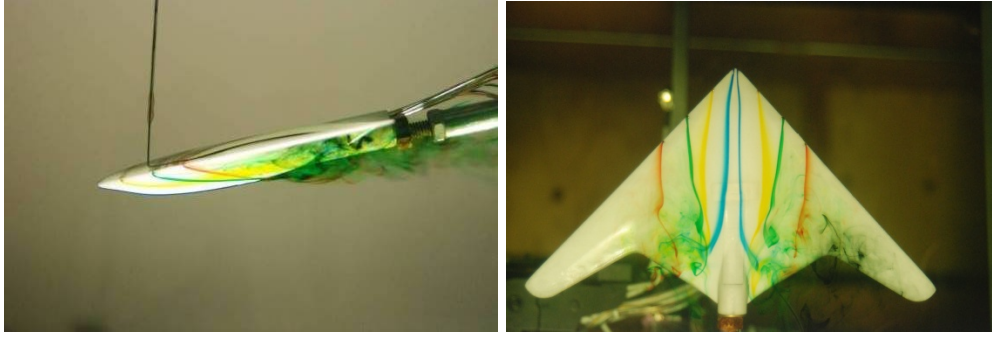
Figure 16 shows a series of dye visualization patterns for Reynolds number of 3.81×10^3 ($U_\infty = 2$ [in/s]) with roll and yaw-angles set to zero and AoA of 2° , 6° and 12° . Figure 16 shows the symmetrical nature of the 1303 UCAV configuration flow at low AoA. The dye showed well-behaved streamlines along the wing surface for $\alpha = 2^\circ$ and $\alpha = 6^\circ$, including the apex streamlines that follow the fuselage until affected by the upstream influence of the support sting. The symmetrical nature of the UCAV 1303 model flow was observed at all flow rates with AoA below those values where leading edge vortical flow structures and associated breakdown began to dominate the flow field typically at $\text{AoA} = 8^\circ$ for $\text{Re} = 1.17 \times 10^4$ ($U_\infty = 6$ [in/s]).



AoA, $\alpha = 2^\circ$



AoA, $\alpha = 6^\circ$



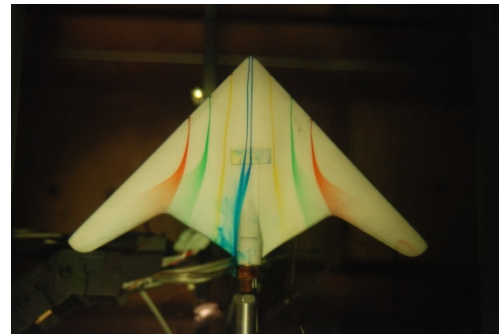
AoA, $\alpha=12^\circ$

Figure 16 Dye Visualization of Flow at $U_\infty=2$ [in/s], $Re=3.81 \times 10^3$

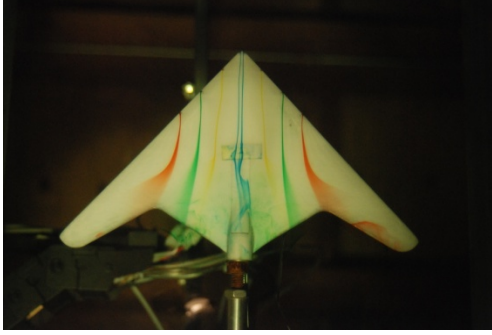
At $\alpha=6^\circ$ the transverse nature of dye flow from mid-plane towards the tip of the wing is observable in Figure 16. Depending on the flow rate under consideration, the dye patterns indicated that flow over the upper surface of the wing was dominated by the spanwise flow developed over the wing for AoA as high as $\alpha=8^\circ$. This characteristic was observed as early as $\alpha=4^\circ$ and is thought to be due to the non-slender (<50 degree leading edge sweep) nature of this wing configuration. The corresponding side view shows that the flow is still very close to the surface over most of the upper surface and has not lifted-off. This was an unexpected result since the flow over a slender delta wing forms leading edge vortices that are distinct by an angle of attack of 8 degrees. As shown in Figure 17, the spanwise flow over the upper surface towards the wing leading edge as marked by the dye was observable at all flow rates investigated. A subtle hint of possible wing tip stall (see red dye) is evident in all these images, even though the angle of attack is small.



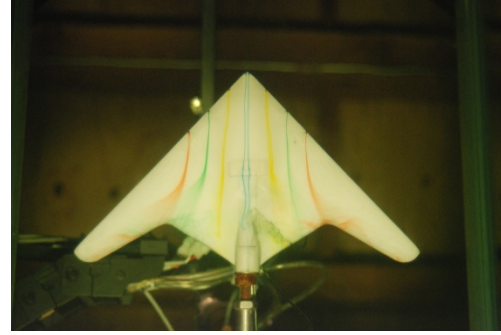
$U_\infty=2$ [in/s], $\alpha=6^\circ$, $Re=3.81 \times 10^3$



$U_\infty=6$ [in/s], $\alpha=6^\circ$, $Re=1.17 \times 10^4$



$U_{\infty}=10$ [in/s], $\alpha=6^{\circ}$, $Re=2.15 \times 10^4$



$U_{\infty}=14$ [in/s], $\alpha=6^{\circ}$, $Re=2.94 \times 10^4$

Figure 17 Transverse Dye Flow Visualization

At $\alpha=12^{\circ}$ LEV flow structures are clearly visible from just aft of mid-chord and progress as a spiraling flow without experiencing breakdown phenomena at the flow conditions of Figure 16, while maintaining well behaved symmetrical flow along the fuselage. Dye streaks are observed to flow inward, towards the fuselage, providing a possible indication of both trailing edge and tip stall. Black dye was clearly observed pooling near the wing tip and trailing edge crank providing further evidence of progressive wing tip stall at $\alpha=12^{\circ}$.

LEV formation was visible as early as $\alpha=8^{\circ}$. At larger AoA and flow rates, the LEVs experience a breakdown phenomenon that drastically alters the flow along the wing upper surface and provides a priori evidence that leading edge vortices were formed. As further indication of the LEV formation, black dye was introduced on the underside of the model to allow visual evidence of the potential flow wrapping around the wing leading edge that leads to vortex roll-up. Figure 18 shows the black dye wrapping from the underside of the model and LEV flow associated with conditions at $U_{\infty}=2$ [in/s] and $\alpha=15^{\circ}$.

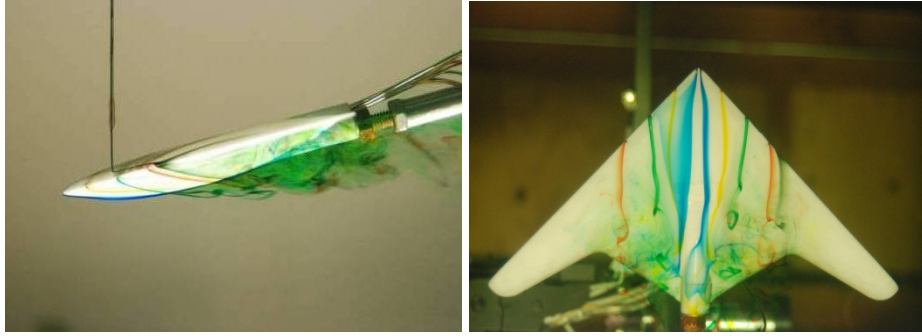


Figure 18 Underside Flow Wrapping, $\alpha=15^\circ$, $U_\infty=2$ [in/s], $Re=3.81 \times 10^3$

One of the major features of the flow around the UCAV model under investigation was the observation of vortex breakdown phenomena. This provided indication of the formation of LEV and also drastically affected the flow around the UCAV. In this investigation, both spiral type and bubble type vortex breakdown were observed, although the spiral mode was the predominant method and was observed with spiral flow occurring just before flow breakdown. Interestingly, bubble and spiral breakdown phenomena could be captured photographically at the same time on the wing (Figure 19), with spiral breakdown clearly visible on the port and starboard sides of the wings and bubble breakdown along the fuselage.

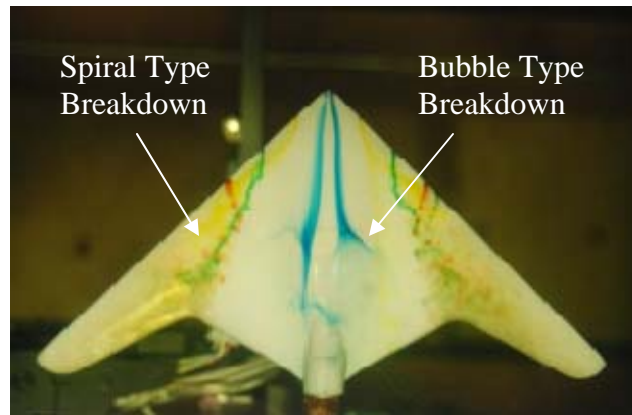


Figure 19 Spiral and Bubble Type Breakdown Phenomena, $\alpha=12^\circ$, $U_\infty=2$ [in/s], $Re=3.81 \times 10^3$

As shown in Figure 16, at $\alpha=12^\circ$ it was also observed that the black dye injected from the starboard underside of the wing has stopped following along the underside of the wing and is now traveling up the topside of the wing providing indication of reverse

flow in the region outboard of the starboard vortex and is indication of possible tip stall. This phenomenon was observed with underside injected dye (black) as early at $\alpha=8^\circ$ for the flow conditions of Figure 16. Reverse flow was also observed for the UCAV model under consideration by placing the external dye port on the starboard topside wingtip. Figure 20 shows the results of this dye flow observation. Here it was clearly observed that the dye flow from the tip has changed direction and has travelled up the topside of the wing, providing further evidence of wing tip stall.

Based on these results, it can be surmised that UCAV 1303 configuration flow is dominated at lower AoA by transverse flow from mid-plane to the wing tip and at higher AoA by leading edge vortex formation on its inboard span and flow separation on the outboard span.

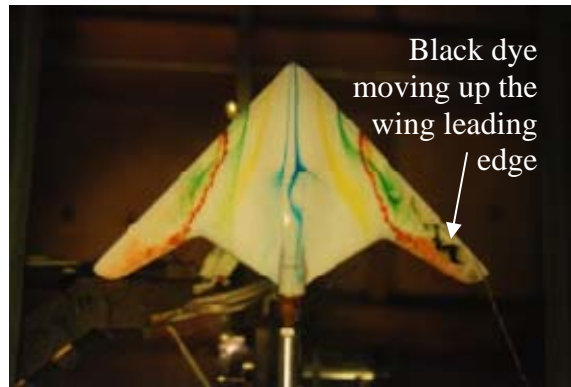


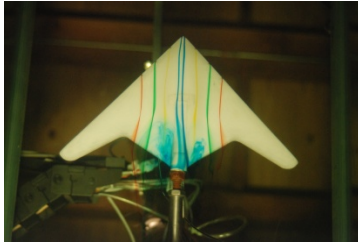
Figure 20 Reverse Flow on UCAV 1303 $\alpha=10^\circ$, $U_\infty=6$ [in/s], $Re=1.17 \times 10^4$

2. Effect of Pitch

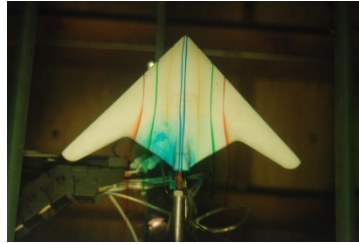
The AoA was varied in an effort to determine the flow field characteristics of the UCAV 1303 configuration during a pitch up maneuver. This was accomplished by establishing a steady flow rate of water over the UCAV model, then photographing the dye flow structure at various AoA. For this investigation, photographs were taken at the angle under investigation and then retaken after first always returning to $\alpha=0^\circ$ to ensure there were no hysteresis effects.

Figure 21 shows a pitch-up sequence for the UCAV model at a constant Reynolds number of 1.17×10^4 . It is observed from these photographs that at AoA below $\alpha=8^\circ$, the flow is dominated by transverse flow from the mid-plane towards the wing tip. Figure 21

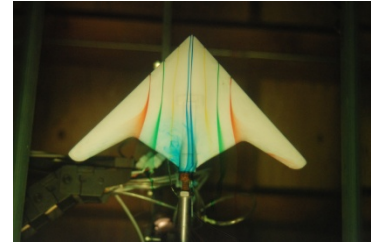
further shows that as AoA is increased below $\alpha=8^\circ$, that the mean cross-flow moves laterally from the inboard crank at $\alpha=0^\circ$ to the wing tip at $\alpha=6^\circ$ and remains symmetrical. It is also observed that the apex streamlines remained well behaved at this flow rate and these pitch conditions.



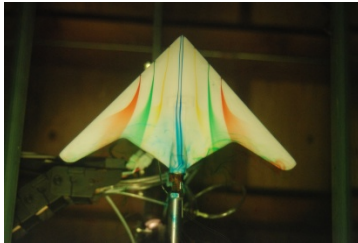
AoA, $\alpha=0^\circ$



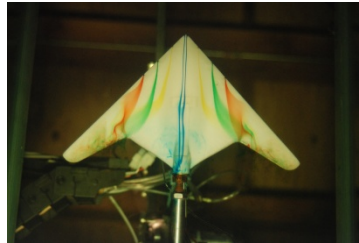
AoA, $\alpha=2^\circ$



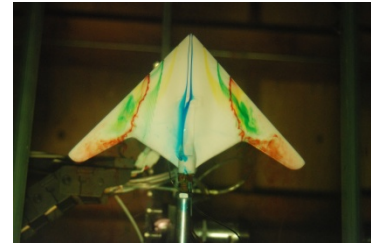
AoA, $\alpha=4^\circ$



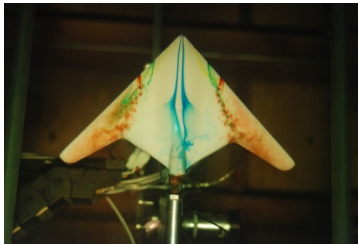
AoA, $\alpha=6^\circ$



AoA, $\alpha=8^\circ$



AoA, $\alpha=10^\circ$



AoA, $\alpha=12^\circ$



AoA, $\alpha=15^\circ$



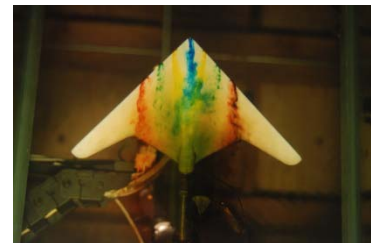
AoA, $\alpha=20^\circ$



AoA, $\alpha=25^\circ$



AoA, $\alpha=30^\circ$



AoA, $\alpha=35^\circ$

Figure 21 Water Tunnel Velocity, $U_\infty=6$ [in/s], $Re=1.17 \times 10^4$

It is observed in Figure 21 that tip stall is visible as early as $\alpha=4^\circ$ and that this region moves upstream and inboard as AoA is increased. Further, as visible by pooling of red dye as AoA is increased, a recirculation region is established at the wing tip providing further evidence of tip stall. A typically observed recirculation flow pattern is highlighted in Figure 22, where $\alpha=12^\circ$. Here, red dye streams in the vortex cores travel to the inboard cranks on both port and starboard sides of the wing then travel outboard to the wing tip before moving up the wing near the leading edge. These results are in close agreement with those presented by Kosoglu and Rockwell [15].

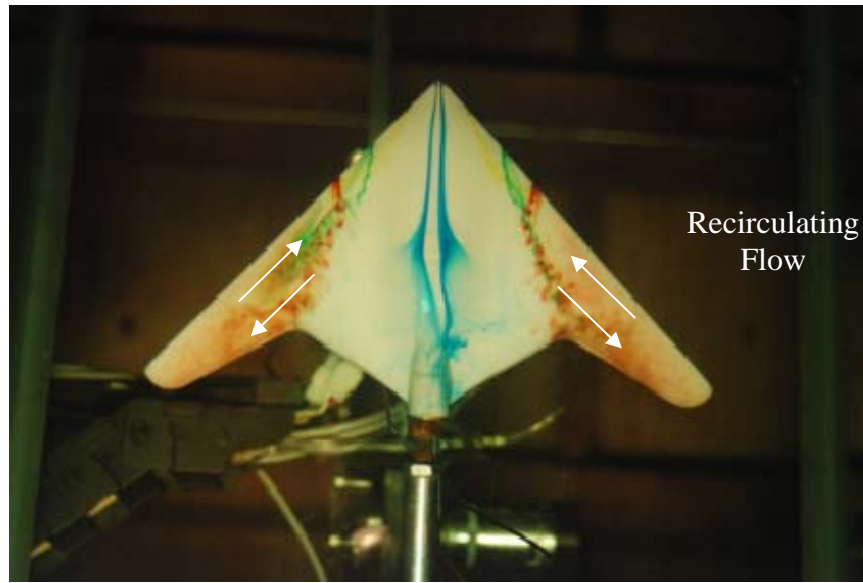


Figure 22 Recirculation Flow Regions, $\alpha=12^\circ$, $U_\infty=6$ [in/s], $Re=1.17 \times 10^4$

As AoA is increased to $\alpha=6^\circ$ in Figure 21, the first evidence of a small vortical flow structure formation becomes visible toward the trailing edge crank?.. This was observed as a slight mixing of the red and green dye streams at the rear of the wing clearly visible in Figure 23. Further increase in AoA beyond $\alpha=6^\circ$, showed that at $\alpha=8^\circ$, the LEV appears to exist in length to approximately $b/4$ in span (inboard crank location) and is observable in both red and green dye flows in Figure 21 [19]. At this AoA, apex flow is no longer completely symmetrical and some flow deviation is observed. By $\alpha=10^\circ$, spiral breakdown was observed in the flow on the outer portion of the wing, while the inner flow has remained undisturbed. Some asymmetry has been introduced in the flow over the fuselage at $\alpha=10^\circ$, as observed by the apparent bubble bursting of flow

over the starboard side of the fuselage with a resultant effect on the wing/body junction flow. As AoA is increased further, $\alpha=12^\circ$ and $\alpha=15^\circ$, it is observed in Figure 21 that flow along the inner portion of the wing is affected, with spiral breakdown observed. Bubble bursting was observed on both sides of the apex flow, with vortical flow in the wing/body junction flow that spread in the lateral direction towards the wing tips. Beyond $\alpha=15^\circ$, complete flow breakdown is observed.

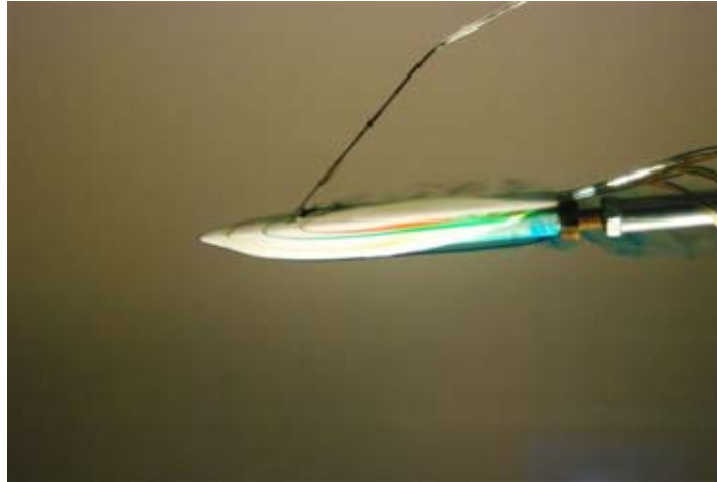


Figure 23 Side View, $\alpha=6^\circ$, $U_\infty=6$ [in/s], $Re=1.17 \times 10^4$

The pitch sequence of Figure 21 shows LEV formation sensitivity to changes in AoA. Based on dye flow observations, exact location of LEV formation was difficult to determine. However, using the dye injection holes as a reference, a qualitative approximation of LEV formation location was possible as AoA was increased beyond $\alpha=8^\circ$, with results listed in Table 4. As an attempt to quantify this information, approximate measurements are provided in Table 4, with an uncertainty of 5%. From this data it is apparent that the LEV formation location moves up the wing as AoA is increased once LEV formation is initiated.

While LEV dominates flow over the outboard sections of the wing, apex streamlines continue to remain well behaved and symmetrical until there is a sudden breakdown in this flow, observed as abrupt bubble type bursting. Vortical flow along the fuselage upstream of breakdown was observed to show some spreading as AoA was

increased. Apex flow breakdown was observed to occur symmetrically and asymmetrically, with no preferential location.

<u>Angle of Attack</u>	<u>Location of LEV Formation</u>
$\alpha=8^\circ$	After the 4 th hole from the apex ($\sim x/c=0.50$)
$\alpha=10^\circ$	Between the 3 rd and 4 th holes from the apex ($\sim x/c=0.25$)
$\alpha=12^\circ$	Between the 2 nd and 3 rd holes from the apex ($\sim x/c=0.15$)
$\alpha=20^\circ$	Between the 1 st and 2 nd holes from the apex ($\sim x/c=0.05$)

Table 4. LEV Formation Location, $Re=1.17 \times 10^4$

It appears that the vortex breakdown begins to occur at the concave trailing edge crank at $\alpha=8^\circ$ in Figure 21. Results also show that the location of vortex breakdown moves as the AoA is increased. Measurement of the vortex bursting location was performed for flow rates between $U_\infty=2$ [in/s] and $U_\infty=14$ [in/s], results for $U_\infty=6$ [in/s] are shown in Figure 24. It is observed that as AoA is increased that the vortex bursting location moves up the wing and follows the general trend as previously published, Lowson and Riley [24], for delta wings with fuselages.

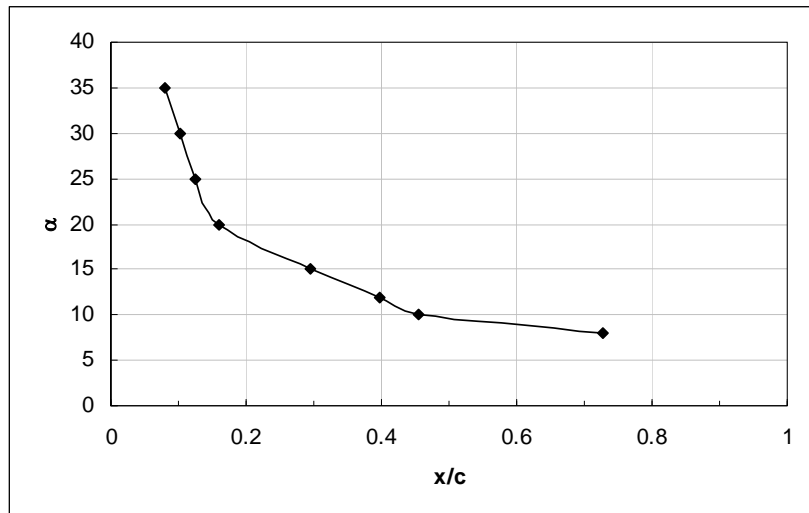


Figure 24 Vortex Breakdown Movement for the UCAV 1303 Configuration, $U_\infty=6$ [in/s], $Re=1.17 \times 10^4$

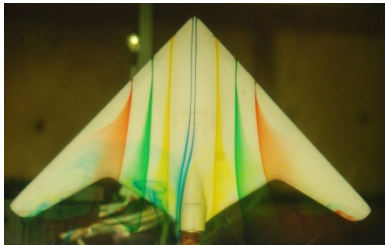
3. Effect of Reynolds Number

The Reynolds number was varied in an effort to determine the flow field characteristics of the UCAV 1303 configuration. This was accomplished by changing the flow rate through the test section of the water tunnel. In this study, flow rate was operated at the nominal values of 2 [in/s], 6 [in/s], 10 [in/s] and 14 [in/s].

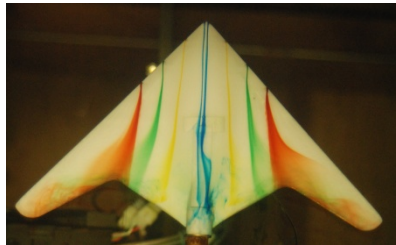
As previously mentioned, the transverse nature of UCAV 1303 flow prior to LEV formation was observed at all flow rates and Reynolds numbers under investigation (Figure 17). It was further observed that for flow conditions prior to LEV formation, apex flow remained symmetrical for all Reynolds numbers under investigation. Differences existed only in the distance along the wing traveled before dye spread and flow turned toward the wing tip. Values measured for the cases of Figure 17, $\alpha=6^\circ$, are tabulated in Table 5 based on flow of the red dye stream

<u>Re</u>	<u>U_∞ [in/s]</u>	<u>x/c</u>
3.81×10^3	2	0.42
1.17×10^4	6	0.48
2.15×10^4	10	0.55
2.94×10^4	14	0.62

Table 5. Reynolds Number Effect on Observable Transverse Dye Flow



$Re=3.81 \times 10^3$



$Re=2.15 \times 10^4$



$Re=2.94 \times 10^4$

Figure 25 Reynolds Number Effect, $\alpha=6^\circ$

Figure 25 shows the effect of Reynolds number at the extremes of water tunnel velocity under investigation. It is observed that signs of tip stall were visible at $\alpha=6^\circ$ for $Re=3.81 \times 10^3$ and that the center of the stall region moved upstream as Reynolds number was increased. It was further observed that the effect of Reynolds number was to promote vortex breakdown. At low Re ($Re=3.81 \times 10^3$) the flow remained well behaved, while at higher Re ($Re=1.17 \times 10^4$) vortex breakdown is clearly observed. Observation also indicated that for flow conditions where LEV formation and bursting has been established, that as Re was increased for the same AoA, that vortex bursting location moved up the wing. This property is easily seen in Figure 26, where bursting location was measured against AoA. Here, the curve shifts to the left as Re is increased. These results follow the general trend observed in research literature by Lowson and Riley [24], whose research was focused on a single Reynolds number, and Kosoglu and Rockwell [15], for flat UCAV 1303 wing shape

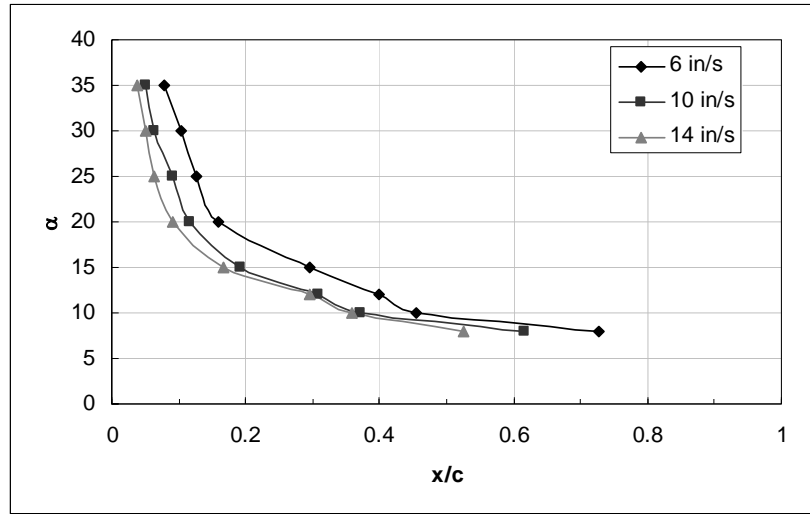
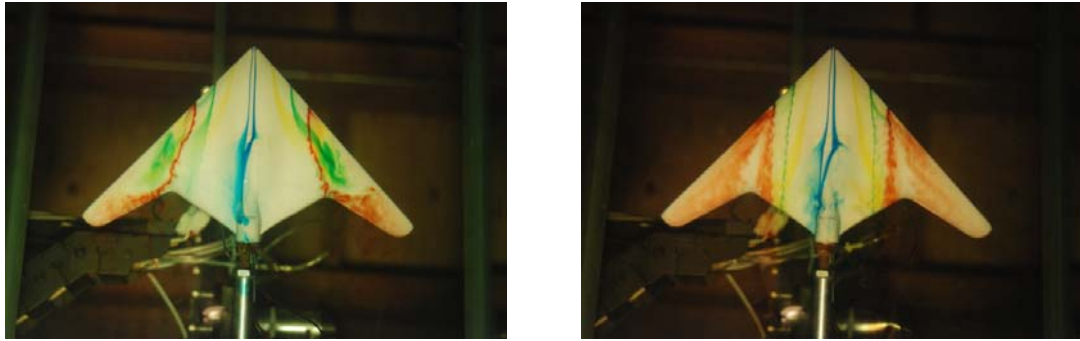


Figure 26 Vortex Breakdown Movement for the UCAV 1303 Configuration for Various Reynolds Numbers

As a further comparison for Reynolds number effects, Figure 27 shows two cases where LEV formation has occurred over a large portion of the wing surface ($\alpha=10^\circ$). It was observed at higher Re , that the dye streams (red, green and yellow) split as a possible indication of secondary vortex formation and that both apex dye flow streams experience bubble type breakdown at approximately the same distance along the fuselage. It was

observed that the trajectory of the vortex core shifted inboard as Reynolds number was decreased, Figure 28, in agreement with literature sources for trends associated with non-slender delta wings. Figure 28 shows evidence of vortex trajectory shift at $\alpha=8^\circ$, $\alpha=10^\circ$ and $\alpha=12^\circ$, with the expected trend observed at each AoA. Compared to literature values, however, the y/s values are slightly higher than those presented by Gursal et al., possibly due to small differences in experimental set-up, model manufacturing or measurement techniques [25].



$U_\infty=6$ [in/s], $Re=1.17 \times 10^4$,

$U_\infty=10$ [in/s], $Re=2.158 \times 10^4$

Figure 27 Reynolds Number Effects with LEV Formation, $\alpha=10^\circ$

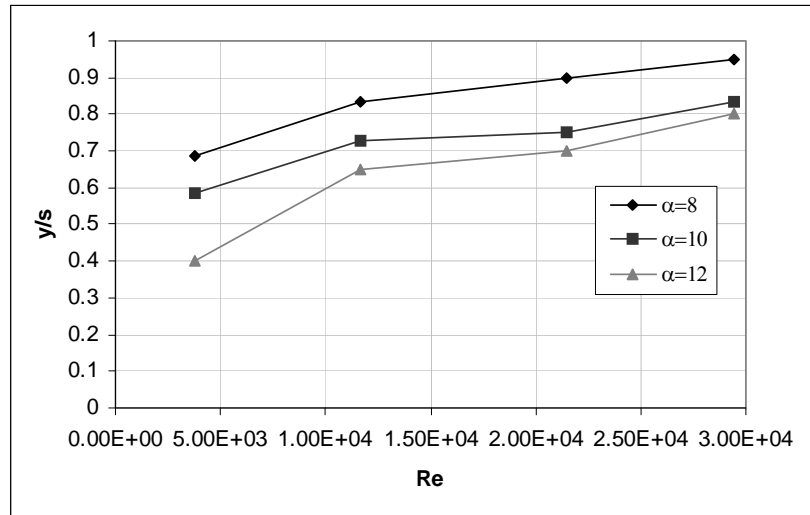


Figure 28 Variation in Spanwise Location of Vortex Core with Re

4. Effect of Roll Angle

The roll angle was varied in an effort to determine the flow field characteristics of the UCAV 1303 configuration during a roll maneuver. This was accomplished by establishing a steady flow rate of water over the UCAV model, then photographing the dye flow structure at various roll angles. Due to the symmetrical nature of the UCAV model, roll effects were investigated in only a single direction. These maneuvers rolled the UCAV model to starboard.

Figure 29 displays the dye visualization for portions of a roll sequence with $U=6$ [in/s], $\alpha=0^\circ$ and $\beta=0^\circ$. The flow at this roll angle is dominated by spanwise flow towards the wingtips, similar to a small angle pitch-up. It is observed that during the roll maneuver that flow symmetry is not maintained, as expected. In the maneuver depicted in Figure 29, it is observed that the spanwise flow normally observed at low AoA is altered. For the roll to starboard side depicted, the normally observed lateral flow from mid-chord is increased on the port side of the wing, while it is retarded on the starboard side of the wing.

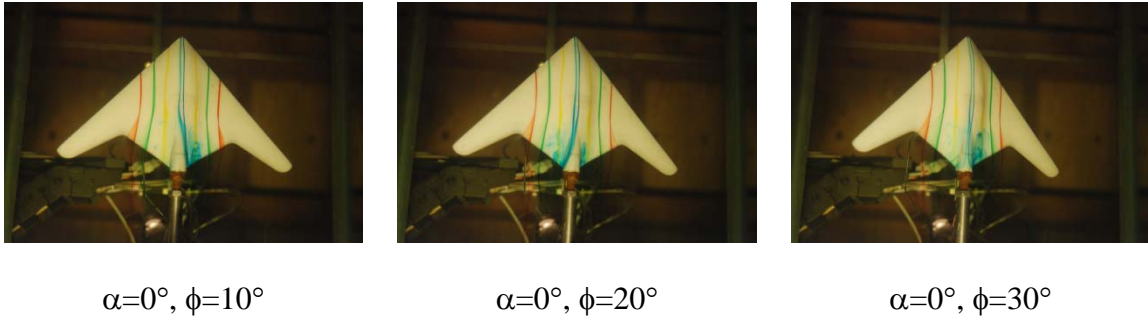
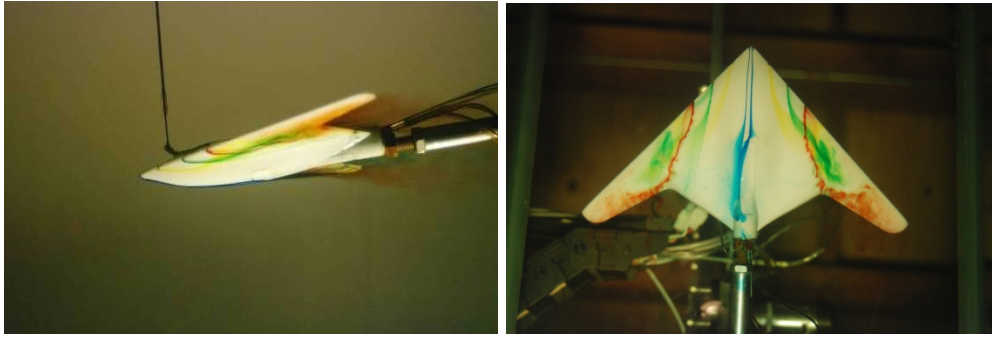


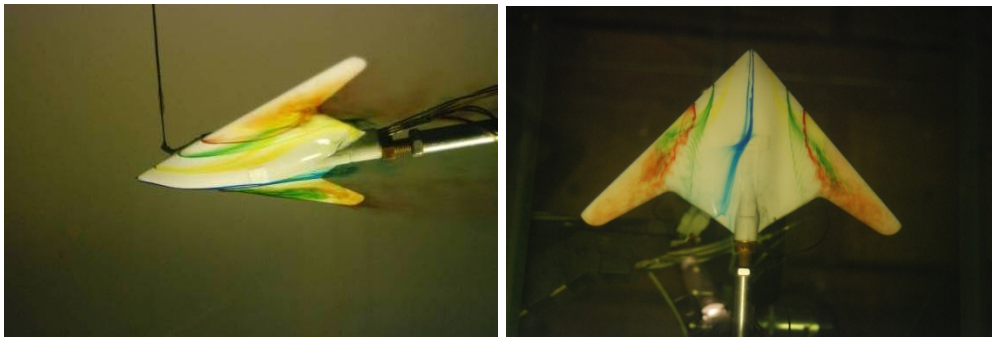
Figure 29 Roll single maneuver, $U_\infty=6$ [in/s], $Re=1.17 \times 10^4$

In an effort to fully realize the effects of roll on the flow structure of the maneuvering UCAV, dye visualizations were taken on the UCAV model under combined maneuvers of pitch and roll. For this investigation, a steady roll angle was applied and pitch varied to see flow field effects. Figure 30 shows the effects of a combined pitch and roll maneuver with $U_\infty=6$ [in/s]. As expected, flow field symmetry was not maintained during combined roll and pitch maneuvers. As roll angle was increased from $\phi=0^\circ$ to $\phi=30^\circ$, it was easily observed that asymmetrical vortex bursting occurred since

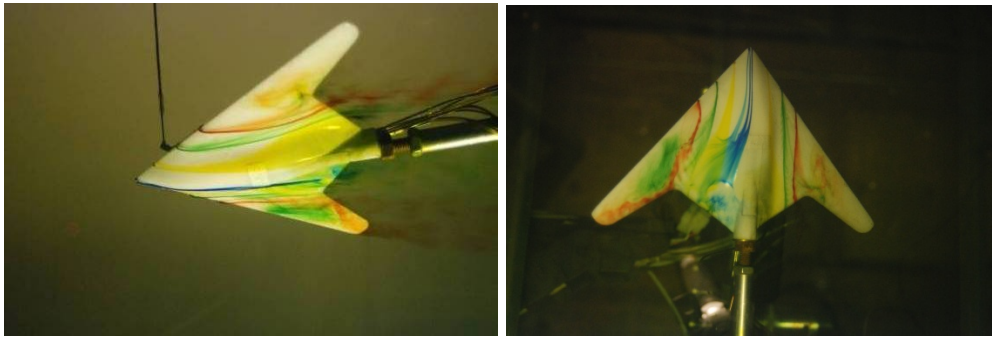
vortex burst locations greatly differed between the two sides of the UCAV wing. It was further observed that as roll angle was increased, that the distance between the vortex burst locations on the wing increased. The flow along the wing away from the roll displayed flow characterized by LEV formation with a relatively small, tight vortical flow structure and vortex bursting that moved up the wing with increased roll angle. The flow along the wing towards the roll displayed flow characterized by LEV formation and vortex bursting that moved down the wing with increased roll angle. Along the wing tips, pooling of dye was observed indicating possible tip stall. Fuselage flow that began with symmetry and traveled along the apex was observed to experience a significant shift with flow pushed away from the roll direction and swept into the inner and outer wing LEV affected flow structures, where it experienced bubble type bursting.



$$\alpha=10^{\circ}, \phi=0^{\circ}$$



$$\alpha=10^{\circ}, \phi=10^{\circ}$$



$$\alpha=10^{\circ}, \phi=30^{\circ}$$

Figure 30 Combined Maneuver, $U_{\infty}=6$ [in/s], $Re=1.17 \times 10^4$

5. Effect of Yaw Angle

The yaw angle was varied in an effort to determine the flow field characteristics of the UCAV 1303 configuration during a yaw maneuver. This was accomplished by establishing a steady flow rate of water over the UCAV model, then photographing the dye flow structure at various yaw angles.

The effect of yaw is to introduce sideslip into the flow around the maneuvering UCAV. Figure 31 displays the results of introducing yaw while operating the UCAV model at $U_\infty=6$ [in/s] with $\alpha=0^\circ$. It is observed that the effect of yaw is to disrupt the expected lateral flow that occurs from mid-chord to wing tip and alters the apex flow along the fuselage.

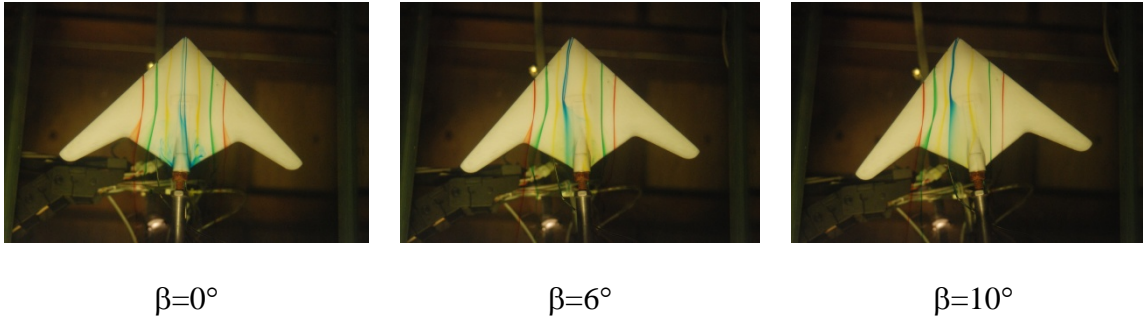


Figure 31 Effect of Yaw, $U_\infty=6$ [in/s], $Re=1.17 \times 10^4$

6. Unsteadiness in LEV Breakdown

Observation of the flow field around the UCAV model proved that a certain degree of unsteadiness existed within the flow field with flow rate, pitch, roll and yaw maintained constant. The unsteadiness was observed as a movement of the LEV bursting location along the wing. With flow rate and pitch maintained constant, an effort to capture the wandering nature of LEV breakdown was undertaken. Figure 32 displays a three second sequence of photographs that clearly display the wandering nature of LEV breakdown. The flow conditions of were $U_\infty=6$ [in/s] and $\alpha=10.5^\circ$, while roll and yaw angles were maintained at zero. In Figure 32, it is observed on the starboard side of the wing that the red and green dye stream vortex bursting locations change along the wing. In this trial, it was observed that the green dye observed vortex bursting location moved as much as $x/c=0.07$ over the three seconds of Figure 31. Further, it was observed that the movement of the vortex bursting locations significantly altered the reverse flow along the wing edges. This value is close to expected values ($0.06c$) for wings of 75° and less as presented by Lowson and Riley [24].

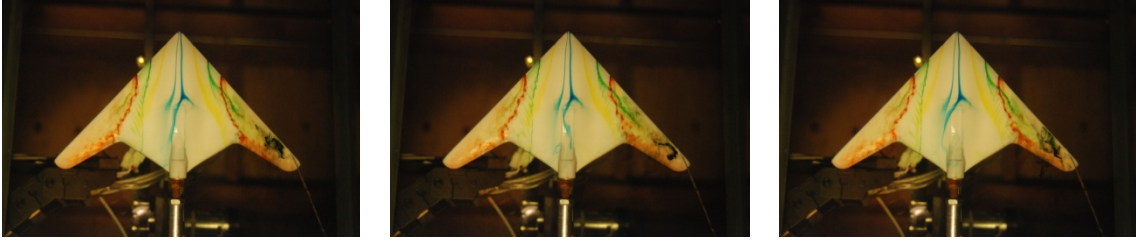


Figure 32 Wandering LEV Breakdown, $U_\infty=6$ [in/s], $\alpha=10.5^\circ$, $Re=1.17 \times 10^4$

C. DYNAMIC MEASUREMENTS

Dynamic flow visualization was performed in an effort to describe the flow field around the UCAV 1303 configuration while the model performed ramp type maneuvers. It is expected that unsteadiness will delay vortex formation, vortex bursting and flow induced stall. The maneuvers of this investigation included pitch-up, roll, yaw and combined pitch and roll maneuvers. During the dynamic runs, the flow field was not allowed to stabilize prior to taking photographic evidence and the model kept maneuvering past the data location at the desired pitch rate, roll rate or yaw rate. To allow comparison between the model of this investigation, other model scales investigated and full scale UCAV 1303 configuration, a non-dimensional pitch rate was utilized for pitch-up maneuvers. The non-dimensional pitch rate, or degree of unsteadiness, is given by Equation (2). A non-dimensional roll rate or yaw rate would be beneficial for scaling, but for this investigation, since roll rate and yaw rate were investigated at a single flow rate, dimensional analysis only was performed.

$$\alpha^+ = \frac{\dot{\alpha} \bar{c}}{U_\infty} \quad (2)$$

1. Effect of Pitch Angle

The pitch angle of the maneuvering UCAV was varied in a ramp type maneuver to investigate dynamic pitch rate effects on the UCAV flow field. For this investigation, the model was pitched from $\alpha=0^\circ$ to $\alpha=30^\circ$, while photographic evidence was taken at the AoA under investigation. The model was then pitched from $\alpha=30^\circ$ to $\alpha=0^\circ$, while

photographic evidence was again taken at the AoA under investigation. The non-dimensional pitch rate was utilized as the standard for this portion of the investigation.

During the pitch-up maneuver, it was observed that the degree of unsteadiness greatly altered the flow field along the UCAV wing. As seen in Figure 33 and Figure 34, for the same AoA and Reynolds number at a lower non-dimensional pitch rate, vortex bursting occurred sooner and had a greater effect on the flow over the outer flow regions of the wing. Here it was observed as a spreading of red dye along the outer wing, spreading towards the wing tip, which may lead to earlier wing tip stall. For the higher non-dimensional pitch rate case, while LEV formation and vortex bursting was not completely prevented, bursting and stall was delayed. Therefore, as the degree of unsteadiness increases, stall is delayed.

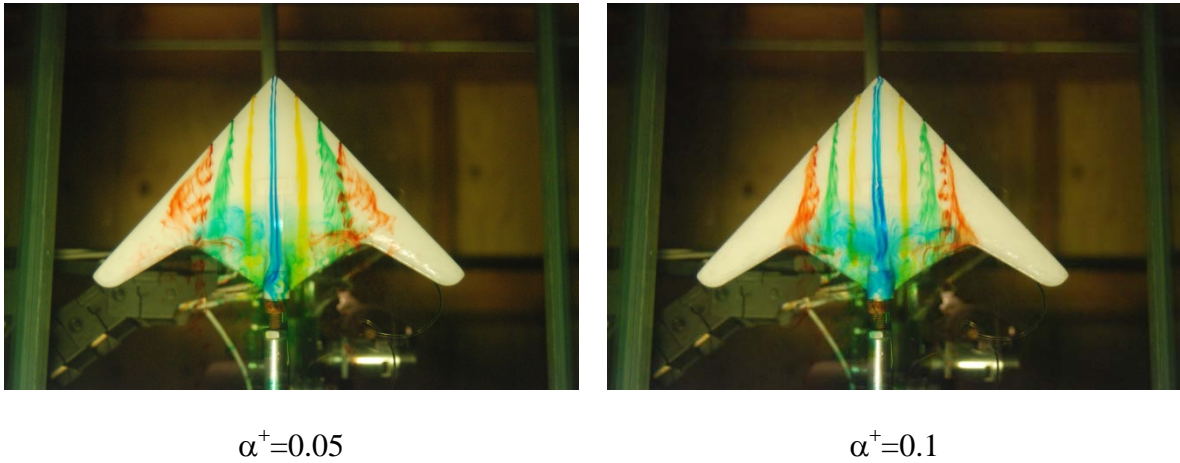


Figure 33 Water Tunnel Velocity, $U_\infty=6$ [in/s], $Re=1.17 \times 10^4$, $\alpha=10^\circ$

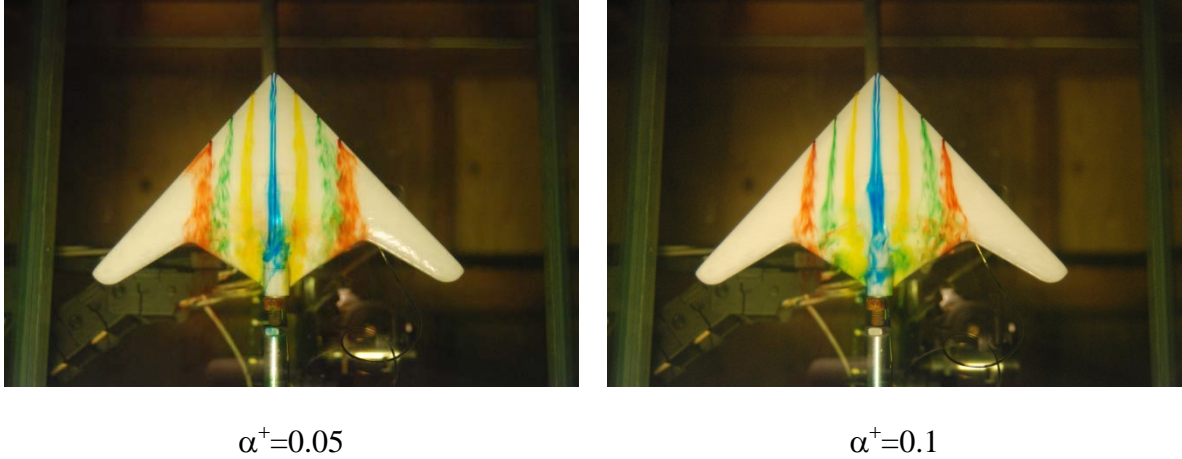


Figure 34 Water Tunnel Velocity, $U_\infty=10$ [in/s], $Re= 2.15 \times 10^4$, $\alpha=10^\circ$

During the pitch-down ramp maneuver from $\alpha=30^\circ$ to $\alpha=0^\circ$, it was observed that flow exhibited a more advanced state of LEV formation, breakdown and flow separation. From Figure 35, it is clearly observed that the flow during the pitch-up maneuver differs significantly from the pitch-down maneuver at the same AoA. During pitch-down maneuver, dye streaks are observed flowing towards the fuselage with vortex bursting occurring inboard of the inner crank at approximately $x/c=0.75$. It is further observed that the amount of vortex bursting and flow separation is significantly greater during the pitch-down maneuver back to $\alpha=0^\circ$, as expected since the model was maneuvered past the AoA where complete flow separation was observed. Fuselage flow remained fairly symmetrical, but bursting was observed at an x/c value much closer to the wing apex at approximately $x/c=0.75$.

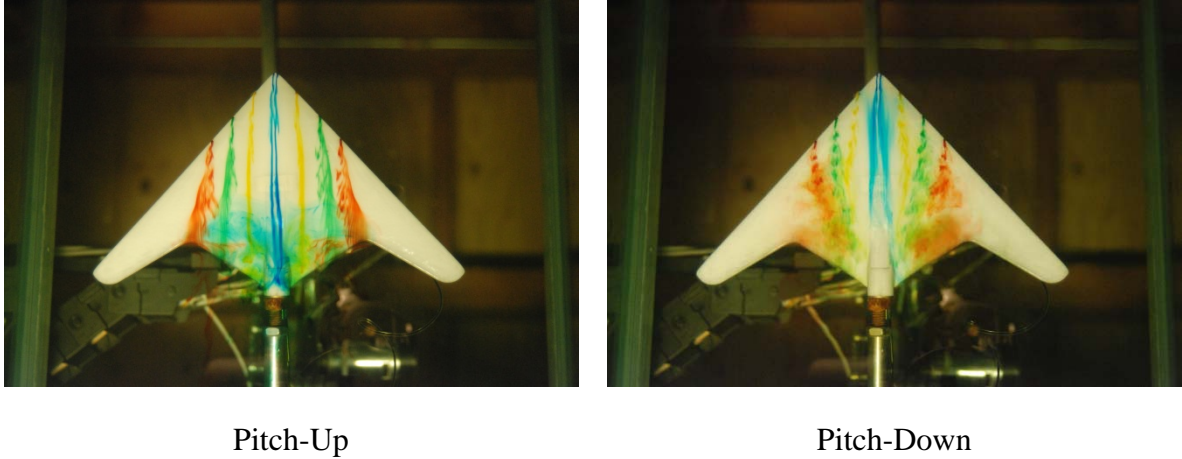
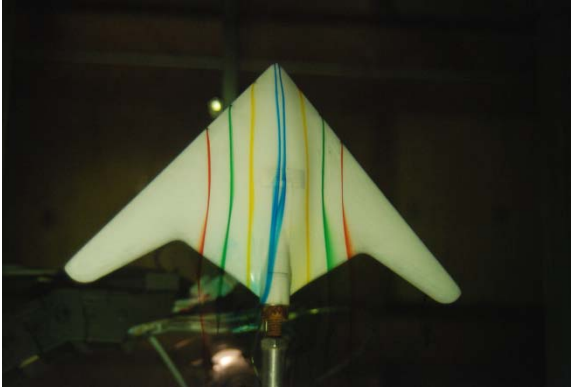


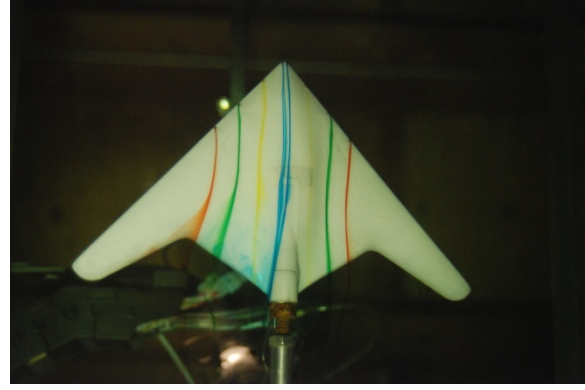
Figure 35 Comparison of Pitch-up and Pitch-Down Maneuver, $U_{\infty}=6$ [in/s], $Re=1.17 \times 10^4$, $\alpha=10^\circ$, $\alpha^+=0.1$

2. Effect of Roll Angle

The roll angle was varied in a ramp type maneuver to investigate dynamic roll rate effects on the maneuvering UCAV flow field. The roll rate investigation was performed at a single water tunnel velocity, and therefore, dimensional roll rate was used for comparison. Figure 36 presents the flow details for the UCAV model at $U=6$ [in/s] with $\alpha=0^\circ$, $\beta=20^\circ$ and the model rolled at roll rates equal to $3^\circ/\text{sec}$ and $10^\circ/\text{sec}$ to starboard. At this roll angle, the flow is dominated by spanwise flow towards the wingtips. It is observed that at higher roll rate, the flow that is along the port side of the UCAV model exhibits a larger lateral velocity, shown as spreading of the red dye stream at the inner crank. Further, at higher roll rate, the dye streams on both port and starboard sides of the wing have shifted, with port flow moving as far as the inner crank and starboard flow dye streams reaching to the wing/body junction. At the flow rates and conditions under investigation, fuselage flow remained well behaved and did not appear to change with changes in roll rate.



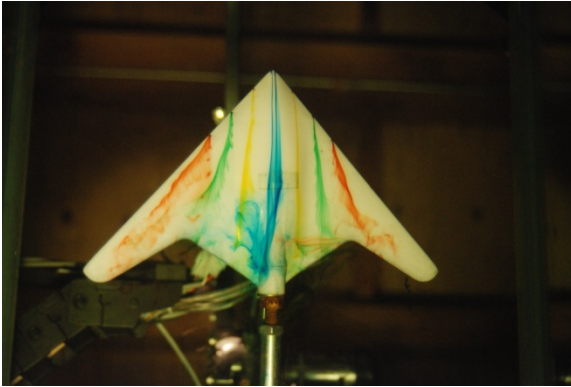
Roll Rate, $\dot{\phi}=3^\circ/\text{s}$



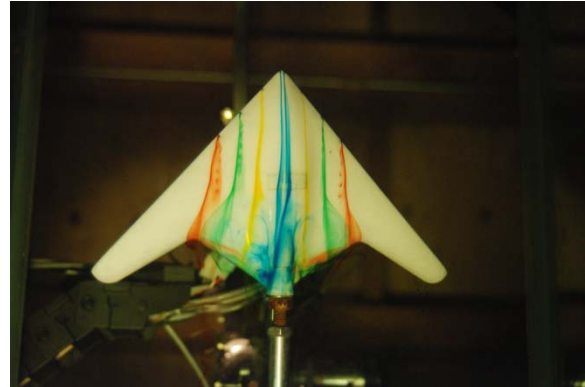
Roll Rate, $\dot{\phi}=10^\circ/\text{s}$

Figure 36 Roll Rate Effects, $U_\infty=6$ [in/s], $Re=1.17 \times 10^4$, $\alpha=0^\circ$, $\phi=20^\circ$ Roll to Starboard

During the combined maneuver investigation, the roll angle was established and the model performed a ramp type pitch-up maneuver. Figure 37 shows typical results of this investigation. At this AoA and roll angle, LEV formation is observable. The higher pitch rate, as with the pitch only maneuver case investigated, has significantly delayed the amount and location of vortex bursting, lowered the amount of flow separation along the outer wing regions and reduced wing tip stall.



Pitch Rate, $\dot{\alpha}=3^\circ/\text{s}$



Pitch Rate, $\dot{\alpha}=7^\circ/\text{s}$

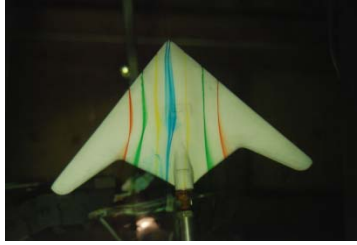
Figure 37 Combined Maneuver, $U_\infty=6$ [in/s], $Re=1.17 \times 10^4$, $\alpha=10^\circ$, $\phi=20^\circ$ Roll to Starboard

3. Effect of Yaw Angle

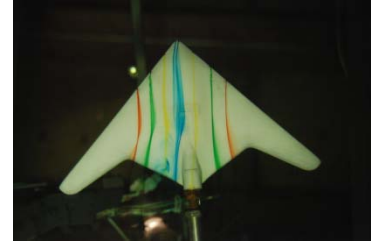
The yaw angle was varied in a ramp type maneuver to investigate dynamic yaw rate effects on the maneuvering UCAV flow field. The yaw rate investigation was performed at a single water tunnel velocity and therefore dimensional yaw rate was used for comparison. Figure 38 presents the flow details for the UCAV model at $U_\infty=6$ [in/s] with $\alpha=0^\circ$, $\beta=6^\circ$ and the model rolled at yaw rates equal to $3^\circ/\text{s}$, $5^\circ/\text{s}$ and $10^\circ/\text{s}$ to port. As with the steady yaw investigation, the flow field is dominated by side-slipping flow that has equally affected all dye streams. It is further observed that there appears to be no affect on the dye streams to changing the yaw rate in this investigation, for the conditions of $U_\infty=6$ [in/s], $\alpha=0^\circ$ and $\beta=6^\circ$. Dye streams appear to be well behaved and flow to the same points along the wing surface.



Yaw Rate, $\dot{\beta}=3^\circ/\text{s}$



Yaw Rate, $\dot{\beta}=5^\circ/\text{s}$



Yaw Rate, $\dot{\beta}=7^\circ/\text{s}$

Figure 38 Yaw Rate Effects, $U_\infty=6$ [in/s], $Re=1.17 \times 10^4$, $\alpha=0^\circ$, $\beta=6^\circ$ Yaw to Port

THIS PAGE INTENTIONALLY LEFT BLANK

IV. LOAD ANALYSIS AND RESULTS

A. LOAD MEASUREMENT

Load measurements were taken using the five-component internal balance during linear and non-linear maneuvers to determine aerodynamic coefficients for the maneuvering UCAV. This technique consisted of using standard procedures to gather strain data during the maneuvers that were converted to equivalent loading using the previously developed calibration output matrix. The strain gages were zeroed at the beginning of each run with the model at $\alpha=0^\circ$ and $\beta=0^\circ$, while a static tare (weight tare) was performed before the actual run that consisted of an angle of attack sweep with the tunnel off ($U_\infty=0$ [in/s]) to eliminate gravitational and inertial effects [21]. Utilization of a five-component internal balance enabled determination of N , S , PM , YM and RM . Therefore, the aerodynamic coefficients C_N , C_M , C_R , C_S , and C_{YM} were able to be computed.

For this investigation, the internal strain gage balance reference center was mounted at $0.53\bar{c}$ aft of the aerodynamic center. Moments calculated during this investigation were transformed and referenced to the aerodynamic center, located at $0.25\bar{c}$ measured from model apex. All forces and moments determined in this investigation are referenced to this point.

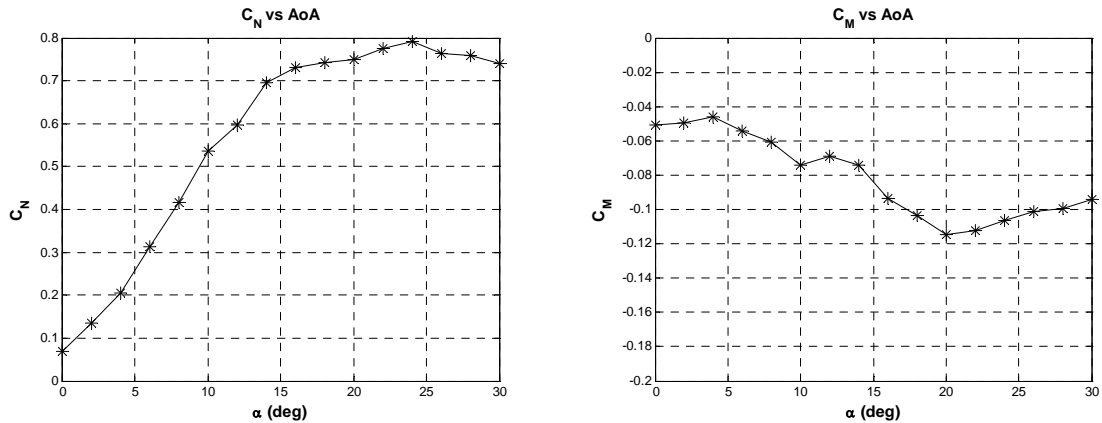
B. STATIC LOADING MEASUREMENTS

As a preliminary investigation, static load measurements on the UCAV 1303 configuration, under various steady flow conditions of Reynolds number, were taken. The tunnel velocity was varied between $U_\infty=2$ [in/s] and $U_\infty=14$ [in/s]. During this investigation, the flow field was permitted time to stabilize after taking zero velocity weight tare measurements and before AoA was adjusted for measurement. The AoA was varied between $\alpha=0^\circ$ and $\alpha=30^\circ$ and was allowed additional time for flow to stabilize before measurements were taken. Tunnel data acquisition/reduction software was utilized with a 1-D sweep testing program to gather static data along the positive AoA sweep axis. Inputs to the 1-D sweep static test program were 360 second flow

stabilization time, twenty second measurement duration time, 100 Hz static sampling frequency and $\Delta\alpha=2^\circ$, angle step increment.

Figure 39 shows results of the AoA variation on the five aerodynamic coefficients under investigation at $U_\infty=6$ [in/s] for AoA sweep of $\alpha=0^\circ$ to $\alpha=30^\circ$. It is observed that the normal force coefficient, C_N , curve behaved approximately linearly from $\alpha=0^\circ$ to $\alpha=14^\circ$, with a slope increase occurring in the range of $\alpha=4^\circ$ to $\alpha=6^\circ$, that is attributable to the increase in importance of vortical flow structures (vortex lift) on the flow field of the maneuvering UCAV 1303 configuration. As AoA was increased beyond $\alpha=14^\circ$, C_N continued to increase $\alpha=24^\circ$, where a maximum in C_N was experienced at a value of $C_N=0.8$. Further increase in AoA resulted in a decrease in C_N , an indication of stall.

The pitching moment coefficient, C_M , reference to the aerodynamic center ($0.25\bar{c}$) curve showed the generally expected trend. C_M started negative, pitch down trend, and remained relatively constant as AoA was increased until vortical flow effects were observed in the range $\alpha=4^\circ$ to $\alpha=6^\circ$ causing a decrease in C_M . As AoA was increased further, vortical flow field effects on the upper surface of the wing resulted in a decrease in C_M to a minimum value of $C_{M,min} = -0.118$ at $\alpha=20^\circ$. After $\alpha=20^\circ$, C_M increased to a less negative value due to the lower pressure experienced on the upper wing surface near the aerodynamic center limiting the tendency to pitch the UCAV wing in the negative pitch direction. These results are in close agreement with results presented by Cunningham and Bushlow [26] that were presented for 3-D and flat plate models.



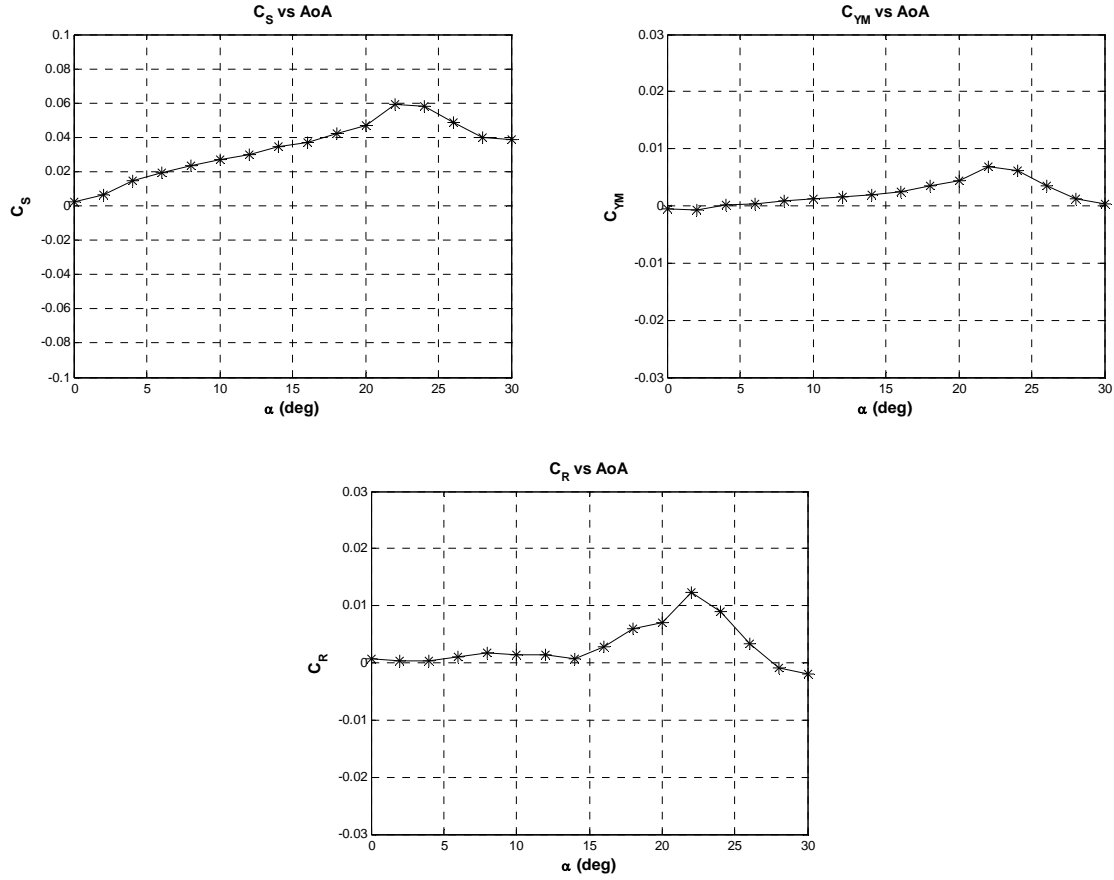


Figure 39 Static Aerodynamic Coefficients, $U_\infty=6$ [in/s], $Re=1.17 \times 10^4$

In the AoA range from $\alpha=0^\circ$ to $\alpha=20^\circ$, unexpected side force variations were observed based on analysis of the side force coefficient, C_s , which may be due to slight sideslip misalignment of the model within the water tunnel from the freestream ($\beta \neq 0$). The values, however, are small. Yawing moment, C_{YM} , and rolling moment, C_R , coefficients are observed to stay very close to zero in the range $\alpha=0^\circ$ to $\alpha=18^\circ$, as expected, for the AoA sweep of this investigation. As AoA is increased above $\alpha=20^\circ$, however, an unexpected increase in C_s , C_{YM} , and C_R are observed, which corresponds to the angle of $C_{M,min}$. The change in C_s , C_{YM} , and C_R is indicative of a change in the flow field effects on the UCAV. At this AoA, the model experienced a side force, yawing and rolling possibly due to asymmetrical vortex bursting that has been typically observed on delta-wing flows and/or unsteadiness in vortex bursting

(chordwise movement of the bursting point at a fixed angle of attack) observed via flow visualization. Figure 40 displays flow field visualization for tunnel velocity at $U_\infty=6$ [in/s] and AoA of $\alpha=15^\circ$, $\alpha=20^\circ$ and $\alpha=25^\circ$ for visual comparison to these results.

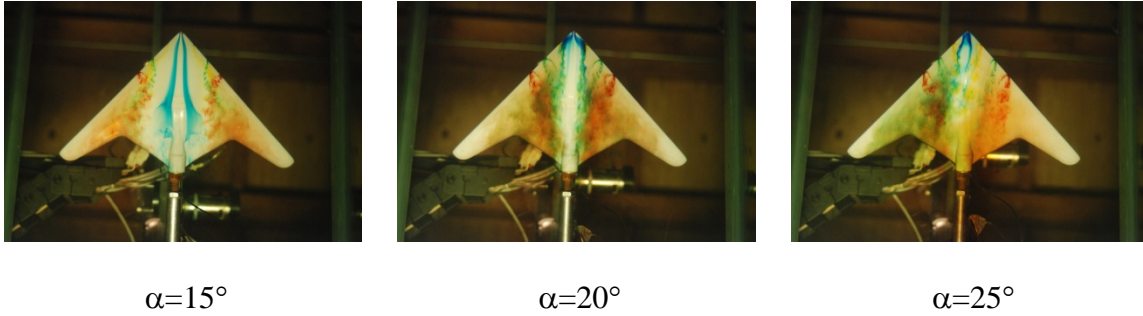


Figure 40 Flow Visualization at Loading Points of Interest, $U_\infty=6$ [in/s], $Re=1.17 \times 10^4$

For comparison, the loading investigation was performed at various Reynolds numbers to determine the effects of Reynolds number on loading measurements. The measurements were made at the same Reynolds numbers utilized for the flow visualization studies and detailed in Table 5 (above). Figure 41 shows the results of the AoA variation on the five aerodynamic coefficients under investigation for AoA sweep of $\alpha=0^\circ$ to $\alpha=30^\circ$. It is observed that for the Reynolds numbers of this investigation, the general trends observed for $U_\infty=6$ [in/s] is followed. Further, while the Reynolds numbers of this investigation are close, there is a discernable trend in C_N , where C_N increases as Reynolds number is increased. C_M values begin higher (less negative), but continue to decrease as AoA is increased above $\alpha=20^\circ$ for increased Reynolds number. Unexpected side forces still exist at the higher Reynolds numbers due to suspected misalignment with the tunnel flow field. Here again, the effect of vortical flow field effects is seen as C_S and C_R show a sudden increase and oscillation at AoA above $\alpha=20^\circ$.

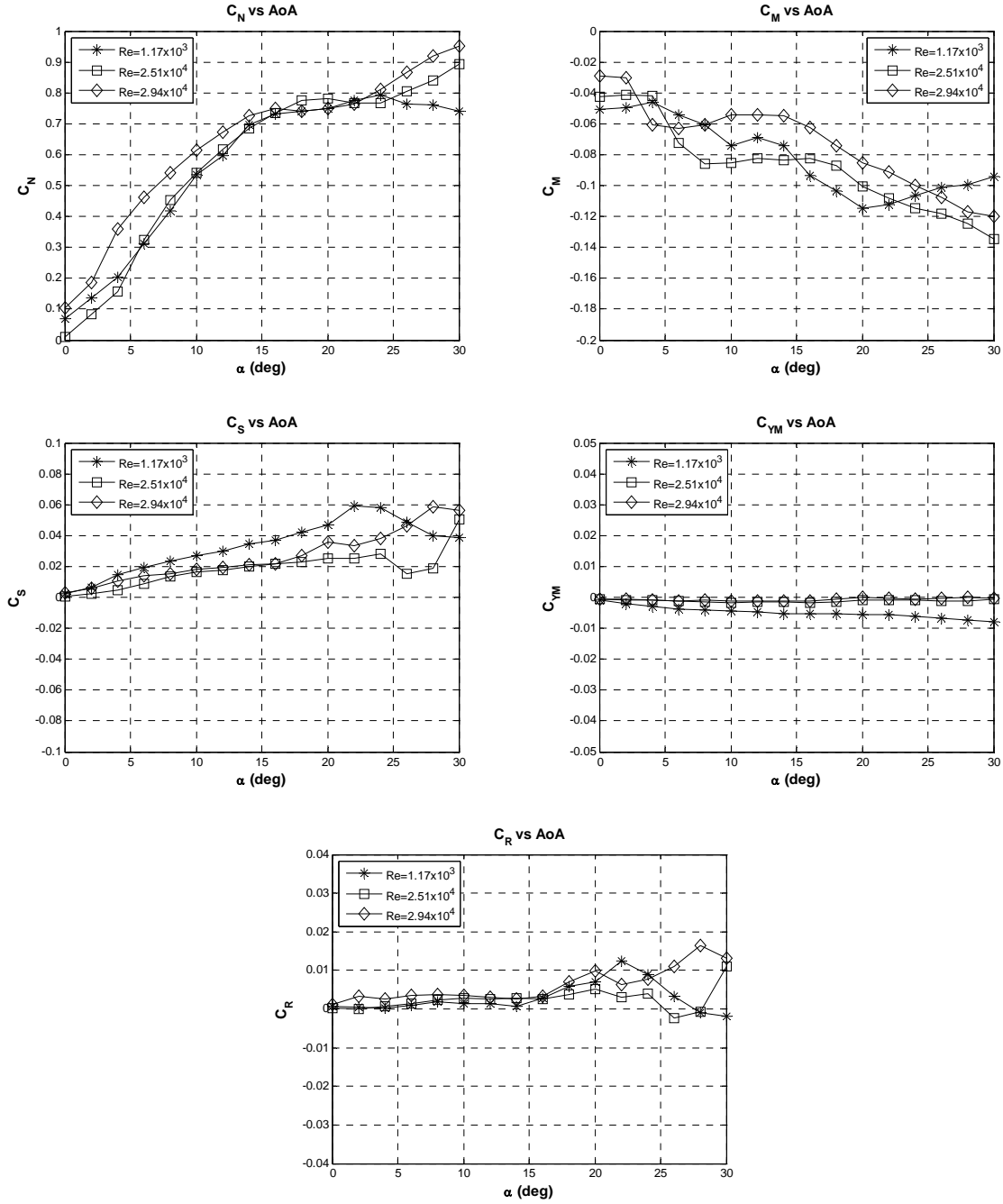


Figure 41 Static Aerodynamic Coefficients Variation with Re

At $Re = 3.81 \times 10^3$ ($U_\infty = 2$ [in/s]), data scatter was observed on aerodynamic force and coefficient moment plots. Even with the very sensitive five-component internal strain gage balance used in this investigation, the extremely small moments measured resulted in voltages hard to distinguish from signal noise and therefore provided

forces/moments and coefficients too small for inclusion in this investigation. For example, the highest normal force value observed at $U_\infty=2$ [in/s] was 0.0063 lb_f, while at $U_\infty=6$ [in/s] it was 0.032 lb_f, a value five times greater.

C. DYNAMIC LOADING MEASUREMENTS

Investigation of the force and moments on the maneuvering UCAV was undertaken to observe the effects in a dynamic maneuver and as a comparison to static data obtained previously. This was accomplished using a forced oscillation maneuver with the model inverted and initially pitched to $\alpha=15^\circ$. Weight tare and static tare information (no flow) was obtained initially to remove gravitational and inertial effects. The maneuver implemented is shown in Figure 42, which is a screen capture of the LABVIEW data acquisition/reduction software used to move the model. In this maneuver, the model was moved to $\alpha=30^\circ$ and full range oscillatory motion began. Maximum pitch rate was established at $\alpha^+=0.1$ and $\alpha^+=0.05$ for the maneuvers of this investigation. Multiple data runs were taken and data averaged to ensure spurious and erroneous signals were removed before data processing. Only pitch up data is discussed in this investigation.

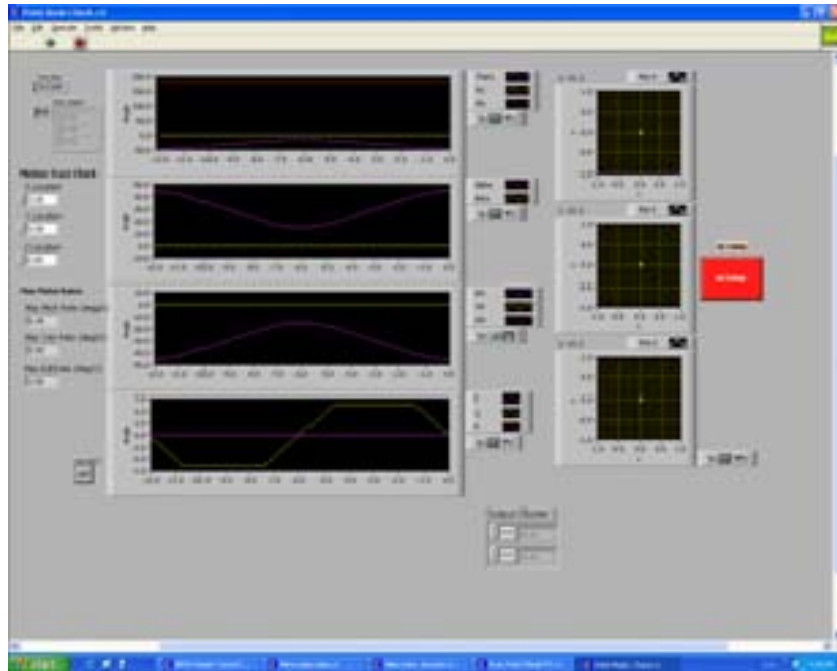


Figure 42 Dynamic Loading Investigation Maneuver, $\alpha^+=0.1$

Figure 43 shows the results of the initial non-dimensional pitch rate under investigation, $\alpha^+=0.1$. It is observed from the results of Figure 43 that as AoA is increased, C_N steadily increases in a nearly linear manner from slightly negative ($C_N = -0.08$) to $C_{N,max}=1.43$. Compared with static data, the C_N value associated with the dynamic investigation is higher, although the general linear shape is consistent with static data. The higher C_N values associated with the dynamic curves is consistent with data presented by Cunningham and Bushlow [26] for delta wing models. This can be attributed to the sustenance of attached flow over the model until higher angles of attack relative to the static case, as has been verified in case of various dynamic stall studies also.

The C_M curve of Figure 43 shows a pitch down trend through the entire range of AoA under investigation. The C_M value showed a slight downward trend as AoA was increased to $\alpha=15^\circ$ in relatively close agreement with the results published for other dynamic studies. Further increase in AoA showed an oscillatory behavior of C_M around a central constant value of approximately $C_M = -0.22$.

C_S , C_{YM} and C_R showed some variation in Figure 43, although the values were small. C_S showed a small increase as AoA was increased that was most likely caused by misalignment of the model within the water tunnel free stream. In contrast to the results of the static investigation, there were no abrupt changes in C_S , C_{YM} or C_R as AoA was increased above $\alpha=15^\circ$.

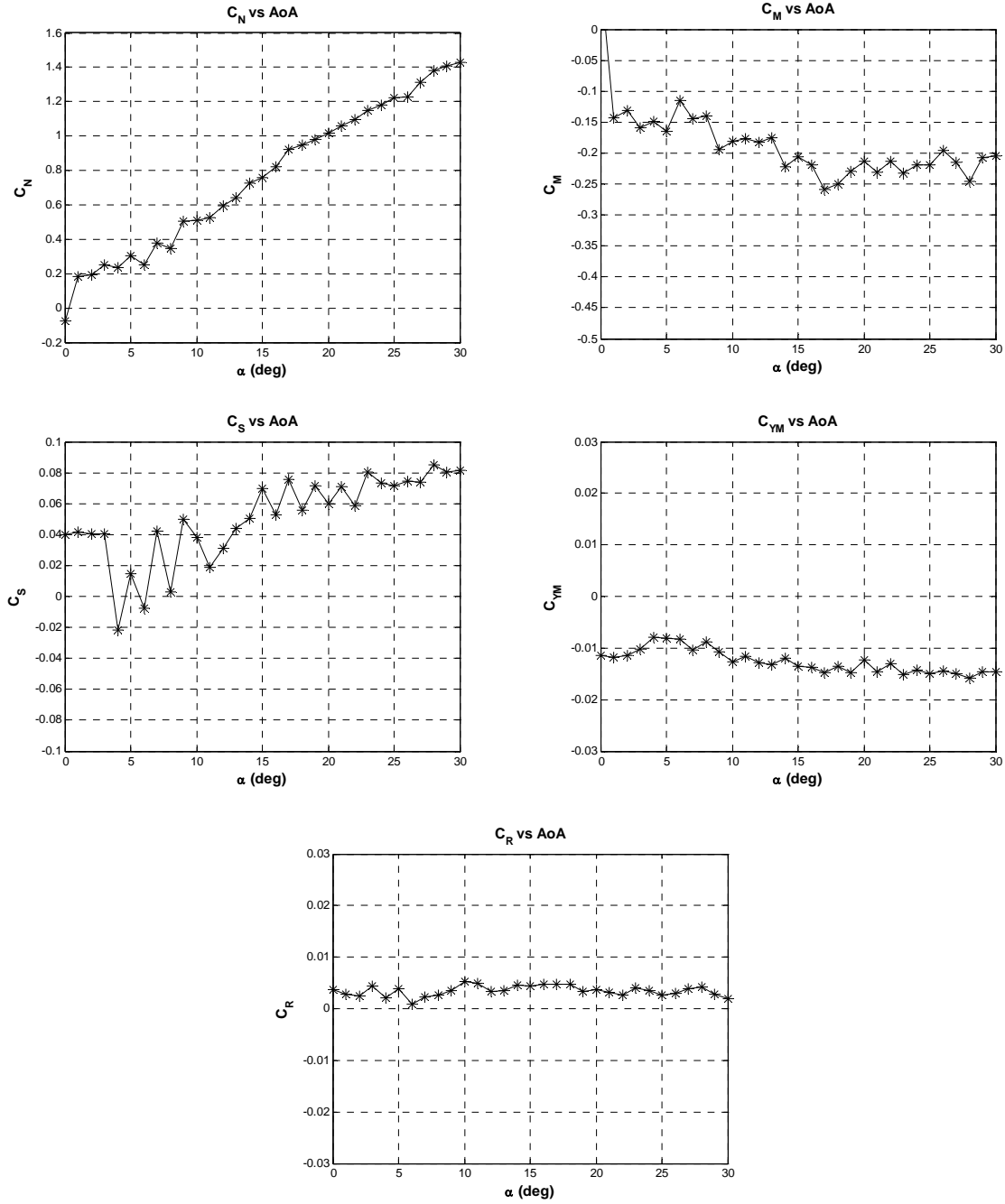


Figure 43 Dynamic Aerodynamic Coefficients, $U_\infty=6$ [in/s], $Re=1.17 \times 10^4$, $\alpha^+=0.1$

Comparison of the dynamic data was made to static data and is presented in Figure 44. Relative to the static data, the dynamic curves are in relatively close agreement with the static curves. For C_N , static and dynamic data are in close agreement to approximately $\alpha=15^\circ$, where a large amount of flow over the UCAV wing has become

fully separated. Here, the dynamic data continues to increase almost linearly to a much higher value of C_N . C_M is in close agreement throughout the range of AoA within this investigation. Interestingly, the C_M are almost collinear after $\alpha=15^\circ$. Again within these curves, C_S and C_{YM} show slight variation as previously addressed and have the same trends for static and dynamic data. In comparison to literature sources, Cunningham and Bushlow [26] show static and dynamic data for a slender delta wing with trends similar to those found in this investigation. Cunningham and Bushlow [26] report that dynamic curves compare well to static data over the alpha range except where full separation is experienced and show dynamic C_N values that peak at higher values than static C_N values.

Within this investigation, initial comparison data was obtained at $\alpha^+=0.05$. While initial results appear promising and track similar expected trends, sluggish system operation during these investigative runs prevented complete investigation and inclusion in this report. A more detailed analysis should be completed at alternative non-dimensional pitch rates to fully describe the dynamic effects on forces and moments experienced by the non-slender UCAV 1303 configuration.

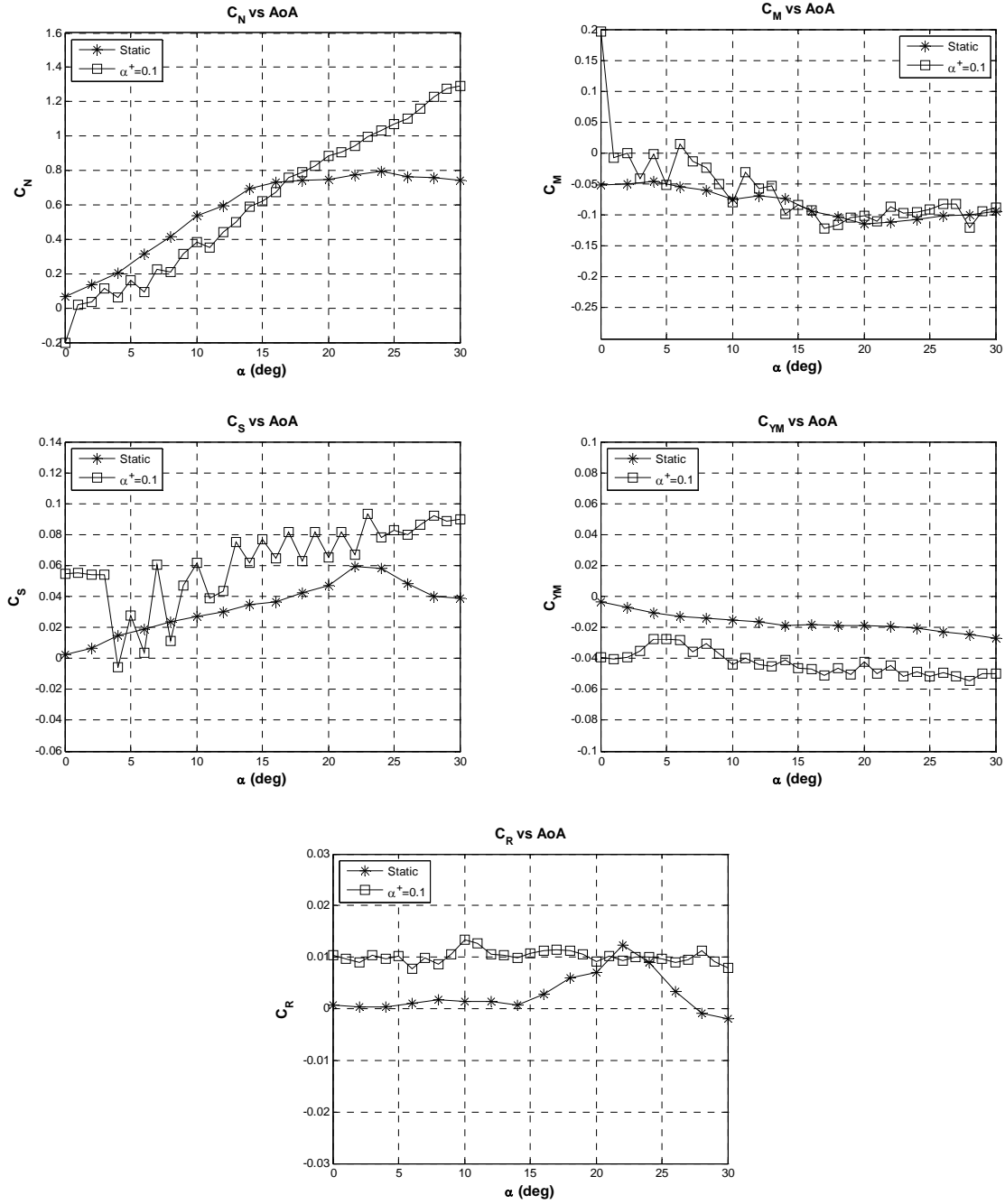


Figure 44 Static and Dynamic ($\alpha^+=0.1$) Coefficient Comparison, $U_\infty=6$ [in/s], $Re=1.17 \times 10^4$

V. CONCLUDING REMARKS

A. SUMMARY OF RESULTS

This study provided a qualitative documentation of the main flow features of a tailless unmanned combat air vehicle (UCAV) through the use of detailed dye flow visualization and photographic techniques for steady and unsteady maneuvers. It further provided preliminary direct measurement of the aerodynamic performance of the low sweep angle delta wing during static and dynamic pitch-up maneuvers.

It was observed that the flow over the UCAV 1303 configuration is complex and is highly dependent on pitch angle, Reynolds number and degree of unsteadiness. Flow was observed to be symmetrical about the central axis and dominated by lateral, spanwise flow from mid-plane to wing tip at low angles of attack ($\alpha < 6^\circ$ for $Re=1.17 \times 10^4$). Flow was also observed to be dominated by vortical flow structure effects that included vortex bursting, vortex bursting location unsteadiness and recirculating flow regions at higher angles of attack ($\alpha > 8^\circ$). Vortex bursting was shown to occur at higher angles of attack with bursting location that moved up the wing surface as AoA was increased and inward as Reynolds number was increased. It was further shown that vortex bursting was delayed as the degree of unsteadiness (non-dimensional pitch rate) increased, which has been shown to delay the onset of stall.

Static load measurements indicated that a maximum in C_N occurred at $\alpha = 24^\circ$. It further indicated the importance of vortex structures on the forces experienced by the low swept delta wing, as observed as a change in slope at approximately $\alpha = 6^\circ$ on the static C_N curve for $Re=1.17 \times 10^4$. C_M was observed to display a pitch down trend as AoA is increased over the entire range of this investigation, with the largest negative value occurring at $\alpha = 20^\circ$. At this angle of attack, C_S , C_{YM} and C_R showed abrupt changes that are perhaps due to the vortical flow structure effects (asymmetrical, unsteady bursting) causing unexpected side forces and rolling moments. These parameters indicate the difficulty of maneuvering the UCAV 1303 as configured at angles beyond some critical angle values. Reynolds number effects were observable in C_N and C_M , as larger values were observed. Dynamic load measurements indicated the degree of unsteadiness

affected the C_N and C_M , while no observable effect was seen during this investigation on C_S , C_{YM} and C_R as would be expected based on static loading data and should be further investigated.

Through this investigation, it was apparent that flow visualization provided a qualitative description of the flow field around the maneuvering UCAV, but that additional methods would be required to obtain a full flow field description. The additional methods include load measurements started in this investigation and would be enhanced by the use of Particle Image Velocimetry or Laser Doppler Velocimetry that could provide instantaneous flow field velocity information (vortical flow structure speed and direction).

B. FUTURE WORK

Future work should focus on measurement of static and dynamic load measurements to further elucidate the flow structure effects on the low swept delta wing. These measurements should include investigation at multiple Reynolds numbers, pitch rates, roll rates and yaw rates with emphasis on acquisition of data runs sufficient to allow ensemble averaging to remove experiment induced effects. Further, these measurements should be compared to the qualitative flow field description of this investigation to ensure an adequate flow field picture is established. Once a fuller picture of the loads is at hand, then its implications on the maneuverability of the UCAV needs to be established subsequent to which, control methodologies must be devised to make it more easily flyable.

LIST OF REFERENCES

- [1] E. C. Wyatt and M. J. Hirschberg, Transforming the Future Battlefield: The DARPA/Air Force Unmanned Combat Air Vehicle (UCAV) Program, AIAA-2003-2616, 2003.
- [2] P. Gasquez, “Uninhabited Combat Air Vehicle Aerodynamics,” MSc Thesis, Cranfield University, England, 2006.
- [3] Predator RW-1/MQ-1/MQ-9 Reaper-Unmanned Aerial Vehicle (UAV)-Air Force Technology, www.airforce-technology.com/projects/predator, July 2009.
- [4] S. C. McParlin, R. J. Bruce, A. G. Hepworth and A. J. Rae, Low Speed Wind Tunnel Tests on the 1303 UCAV Concept, AIAA-2006-2985, 2006.
- [5] M. V. Ol, Water Tunnel Velocimetry Results for the 1303 UCAV Configuration, AIAA-2006-2990, 2006.
- [6] S. J. Woolvin, A Conceptual Design Study of the 1303 UCAV Configuration, AIAA-2006-2991, 2006.
- [7] G. M. Billman, and B. A. Osborne, High L/D Extended Range/Range – Fighter Aircraft Technology – Final Report, 1998.
- [8] M. Atkinson and F. Ferguson, A Computational Fluid Dynamics Investigation of the 1303 UCAV Configuration with Deployable Rao Vortex Flaps, AIAA-2006-1202, 2006.
- [9] J. D. Anderson, “Fundamentals of Aerodynamics,” 3rd ed., McGraw-Hill Publishing Company, 2001.
- [10] F. M. Payne, T. Terry, and R. C. Nelson, Visualization of Leading Edge Vortices on a Series of Flat Plate Delta Wings, NASA Contractor Report 4320, 1991.
- [11] C. D. Munro, P. Krus and C. Jouannet, Implications of Scale Effect for the Predication of High Angle of Attack Aerodynamics, Progress in Aerospace Sciences, Volume 41, 2005, pp. 301-322.
- [12] T. Sarpkaya, Vortex Breakdown and Turbulence, AIAA-1995-0433, 1995.
- [13] D. I. Greenwell, A Simple Engineering Model for Vortex Breakdown, AIAA-2003-3943, 2003.
- [14] R. C. Nelson, T. C. Corke, C. He, H. Othman, and T. Matsuno, Modification of the Flow Structure over a UAV Wing for Roll Control, AIAA 2007-0884.

- [15] D. Rockwell, Origin and Control of the Flow Structure on Unmanned Combat Air Vehicles, AFRL Report SFRL-SR-AR-TR-08-0110, January 2008.
- [16] F. Zhang, M. Khalid and N. Ball, A CFD Based Study of UCAV 1303 Model, AIAA 2005-4615.
- [17] M. D. Wong and J. Flores, Application of OVERFLOW-MLP to the Analysis of the 1303 UCAV, AIAA 2006-2987.
- [18] J. J. Chung and T. Ghee, Numerical Investigation of UCAV 1303 Configuration with and without Simple Deployable Vortex Flaps.
- [19] H. M. Kwon, "Water Tunnel Flow Visualization Studies of Canard-Configured X-31 A-like Fighter Aircraft Model," Naval Postgraduate School, 1990.
- [20] W. H. Chua, "Flow Visualization Studies Over a UCAV 1303 Model," Naval Postgraduate School, 2009.
- [21] C. J. Suarez and B. F. Ayers, Force and Moment Measurements in a Flow Visualization Water Tunnel, AIAA-94-0673.
- [22] C. J. Suarez and B. F. Ayers, Water Tunnel Force and Moment Measurements on an F/A-18, AIAA-94-1802-CP.
- [23] C. J. Suarez and B.F. Ayers, Dynamic Water Tunnel Tests Flow Visualization and Force/Moment Measurements on Maneuvering Aircraft, AIAA-95-1843-CP.
- [24] M. V. Lowson and A. J. Riley, Vortex Breakdown Control by Delta Wing Geometry, AIAA-94-3487-CP.
- [25] I. Gursal, R. Gordinier and M. Visbal, Unsteady Aerodynamics of Nonslender Delta Wings, Progress in Aerospace Sciences, Volume 41, 2005, pp. 515-557.
- [26] A. M. Cunningham, Jr. and T. Bushlow, Steady and Unsteady Force Testing of Fighter Aircraft Models in a Water Tunnel, AIAA-90-2815-CP.

INITIAL DISTRIBUTION LIST

1. Defense Technical Information Center
Ft. Belvoir, Virginia
2. Dudley Knox Library
Naval Postgraduate School
Monterey, California
3. Professor M.S.Chandrasekhara
Department of Mechanical and Astronautical Engineering
NASA Ames Research Center, M.S. 215-1
Moffett Field, California